

DP-FedAdamW: An Efficient Optimizer for Differentially Private Federated Large Models

Jin Liu Yinbin Miao Ning Xi

School of Cyber Engineering, Xidian University, Xi'an, China

{jinliu9787, ybmiao, nxi}@xidian.edu.cn

Junkang Liu

College of Intelligence and Computing, Tianjin University, Tianjin, China

junkangliukk@gmail.com

Abstract

Balancing convergence efficiency and robustness under Differential Privacy (DP) is a central challenge in Federated Learning (FL). While AdamW accelerates training and fine-tuning in large-scale models, we find that directly applying it to Differentially Private FL (DPFL) suffers from three major issues: (i) data heterogeneity and privacy noise jointly amplify the variance of second-moment estimator, (ii) DP perturbations bias the second-moment estimator, and (iii) DP amplify AdamW’s sensitivity to local overfitting, worsening client drift. We propose DP-FedAdamW, the first AdamW-based optimizer for DPFL. It restores AdamW under DP by stabilizing second-moment variance, removing DP-induced bias, and aligning local updates to the global descent to curb client drift. Theoretically, we establish an unbiased second-moment estimator and prove a linearly accelerated convergence rate without any heterogeneity assumption, while providing tighter (ϵ, δ) -DP guarantees. Our empirical results demonstrate the effectiveness of DP-FedAdamW across language and vision Transformers and ResNet-18. On Tiny-ImageNet (Swin-Base, $\epsilon = 1$), DP-FedAdamW outperforms the state-of-the-art (SOTA) by 5.83%. The code is available in Appendix.

1. Introduction

As data volumes surge and privacy concerns grow, centralized learning methods are facing increasing limitations in terms of security and collaboration. Federated Learning (FL) [49] enables decentralized training without sharing raw data, reducing privacy risks [7]. However, FL model updates remain vulnerable to attacks [12, 71, 72]. Differential Privacy (DP) [10] provides formal protection by adding noise, but this increases gradient variance and hinders convergence, especially under non-IID data [22].

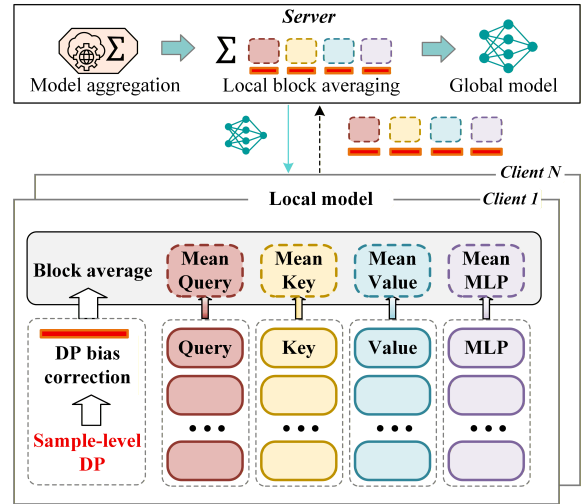


Figure 1. Illustration of our DP-FedAdamW. It aggregates the mean of block-wise Bias-Corrected second moment estimates and performs local–global alignment to stabilize DPFL optimization.

The emergence of large-scale models such as Swin Transformer [47], BERT [26], and GPT [2] has become dominant in vision and language tasks. These deep, parameter-heavy models are highly sensitive to optimization settings, which not only affects training stability but also impacts overall performance. Most DPFL algorithms are built upon the SGD optimizer and adopt the DPSGD [1] mechanism for privacy preservation [23, 24, 52, 73]. While effective for small-scale networks, DPSGD becomes inefficient for large Transformer models as the combination of gradient clipping and injected noise severely distorts gradients, amplifying instability and slowing convergence.

In the pursuit of more efficient optimizers, adaptive methods like AdamW [48] have become state-of-the-art (SOTA) in deep learning. By decoupling weight decay from adaptive moment estimation, AdamW provides enhanced

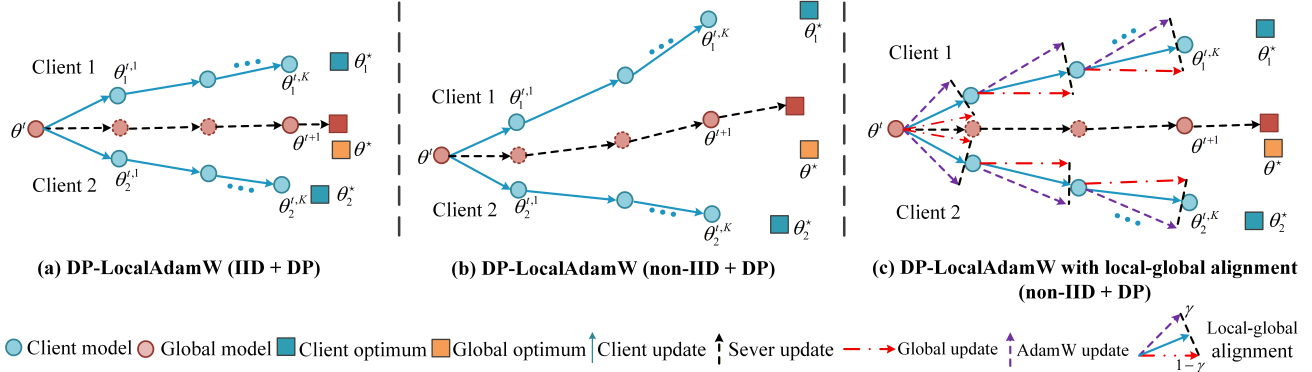


Figure 2. An illustration of local update in DP-FedAdamW, which corrects client drift caused through global update guidance.

stability and generalization, making it a compelling choice for various machine learning tasks. These advantages make AdamW a promising candidate for DPFL, where privacy and robustness are crucial. However, our experiments reveal that AdamW fails to deliver its usual benefits in the DPFL setting. In some cases, its performance is comparable to or even worse than SGD. As illustrated in Table 2, when AdamW is applied locally without any modifications (referred to as DP-LocalAdamW), its performance on the Swin-Tiny model (CIFAR-100, Dirichlet distribution $\alpha=0.1$) is worse than DP-FedAvg-LS. These findings suggest that AdamW struggles with the challenges posed by privacy constraints and decentralized FL.

Challenges. We identify three main challenges that contribute to the unexpected results. (i) **Second-moment estimator variance amplification.** Non-IID client data and DP noise jointly inflate the variance of the second-moment estimator, leading to unstable adaptive scaling in AdamW. (ii) **Bias in second-moment estimator.** Gradient clipping and noise injection introduce a systematic bias in the second-moment estimator of AdamW. (iii) **Client drift.** Under non-IID data, DP clipping and noise amplify AdamW’s sensitivity to local overfitting, further worsening client drift. All challenges are explored in more detail in Section 4. These findings raise a key question: **How can AdamW maintain effectiveness in the presence of differential privacy and federated heterogeneity?**

To answer this, we propose DP-FedAdamW, a new differentially private adaptive optimizer that restores the effectiveness of AdamW under non-IID data and privacy noise. DP-FedAdamW (i) aggregates second-moment estimates in a block-wise manner to stabilize variance and improve communication efficiency, (ii) eliminates DP-induced bias through an unbiased second-moment correction, and (iii) enforces local–global update alignment to mitigate client drift, achieving more stable and accurate convergence.

Our contributions are summarized as follows:

- **Empirical importance of AdamW and challenges in DPFL.** We empirically demonstrate the effectiveness of

AdamW in DPFL. Our analysis reveals three key challenges: high variance in second-moment estimator, bias in second-moment estimator, and high client drift.

- **DP-FedAdamW: A principled adaptive optimizer for DPFL.** We propose DP-FedAdamW, a communication-efficient DPFL algorithm. It integrates global update estimation into local updates to suppress client drift, aggregates block-wise means of second-moment statistics across clients to stabilize variance, and introduces a Bias-Corrected mechanism to eliminate second-moment estimation bias caused by DP.
- **Theoretical and empirical guarantees.** We derive the first convergence guarantee for a DPFL adaptive optimizer that overcomes gradient heterogeneity, achieving a linear speedup rate of $\mathcal{O}(\sqrt{(L\Delta\sigma_1^2)/(SKT\epsilon^2)} + (L\Delta)/T + \sigma^2 G_g^2/s^2 R^2)$. Experiments on vision and language benchmarks demonstrate that DP-FedAdamW achieves a better privacy–utility trade-off and consistently outperforms SOTA DPFL baselines in convergence.

2. Related work

Differentially Private Federated Learning (DPFL). We adopt sample-level DP for FL, ensuring privacy for each training example against any observer of the updates (the server or third parties). The most prevalent DP-FedAvg [52] applies per-sample clipping and Gaussian noise locally before aggregation. DP-SCAFFOLD [52] introduces control variates to alleviate client drift under privacy constraints. DP-FedAvg-LS [34] improves performance using Laplacian smoothing [53]. Beyond SGD, DP-FedSAM [62] uses Sharpness-Aware Minimization (SAM [21]) to find flatter minima, improving robustness to DP noise. Despite progress in refined clipping and personalized DP [37, 68], optimization remains the dominant bottleneck. However, these algorithms all employ the SGD optimizer for local updates and do not consider the use of adaptive optimizers. In the optimization of large-scale models, the AdamW optimizer has been shown to outperform SGD significantly in both convergence speed and final perfor-

Table 1. Comparison with existing DPFL optimizers.

Method	DP-FedAvg	DP-SCAFFOLD	DP-FedSAM	DP-LocalAdamW	DP-FedAdamW
Optimizer Type	SGD	SGD	SAM	AdamW	AdamW
Scalability to Large Models	Limited	Limited	Moderate	Moderate	High
Client Drift	Strong	Weakened	Slightly weakened	Slightly weakened	Weakened
Communication Cost	1×	2×	2×	1×	1×

mance [3–5, 8, 9, 13–20, 31–33, 35, 36, 45, 46, 50, 54–56, 60, 61, 63, 64, 66, 75–77].

Adaptive optimization. Adaptive optimizers such as Adam [27], AdamW [48], AMSGrad [58], Amsgrad [57] adapt per-parameter step sizes from gradient history, achieving faster and more stable convergence than vanilla SGD and becoming standard for large models (e.g., Transformers) [29, 74]. Among these, AdamW applies weight decay directly on parameters, preventing undesired interaction between regularization and moment adaptation, thus improving convergence and generalization [38–40, 48, 70]. **Adaptive optimization in Federated Learning.** A line of work brings adaptive updates into FL. FedOpt [59] introduces server-side adaptivity, instantiating Adam and Yogi at the aggregator. FAFED [69] stabilizes training by aggregating clients’ first- and second-moment estimates of Adam. FedAMS [6] highlights that averaging the second-moment is pivotal to avoid divergence. FedLADA [65] aggregates the second-moment estimate to reduce communication cost. However, these studies mainly evaluate on CNNs. However, these algorithms do not take into account the impact of noise introduced by DP. FedBCGD [38] proposes an accelerated block coordinate gradient descent framework for FL. FedSWA [39] improves generalization under highly heterogeneous data by stochastic weight averaging. FedAdamW [43] introduces a communication-efficient AdamW-style optimizer tailored for federated large models. FedNSAM [41] studies the consistency relationship between local and global flatness in FL. FedMuon [42] accelerates federated optimization via matrix orthogonalization. DP-FedPGN [44] develops a penalizes gradient norms to encourage globally flatter minima in DP-FL.

Our contributions. To the best of our knowledge, adaptive optimization has not yet been systematically explored in the context of DPFL. Existing DPFL optimizers still struggle to train large models in a stable and efficient manner. To address this gap, we propose a method that stabilizes second-moment statistics via block-wise aggregation, removes DP-induced bias in the second moment, and aligns local updates with an estimated global descent direction in a communication-efficient way. We summarize representative DPFL methods and their characteristics in Table 1.

3. DPFL framework

Consider a general DPFL system with N clients. The FL objective is to minimize the following population risk:

$$f(\theta) = \frac{1}{N} \sum_{i=1}^N f_i(\theta), f_i(\theta) := \mathbb{E}_{\xi_i \sim \mathcal{P}_i} [F_i(\theta; \xi_i)], \quad (1)$$

where f_i is the loss function of client i . ξ_i is drawn from distribution \mathcal{P}_i in client i , and $\mathbb{E}[\cdot]$ denotes expectation with respect to the sample ξ_i .

In communication round t , the server selects S clients and distributes the global model θ^t . The client i computes the gradient for each sample j in local k iterations (with a mini-batch $\mathcal{D}_i^k = \lfloor sR \rfloor$, s is data sampling rate, R is number of client samples): $g_{ij} = \nabla f_i(\theta_i^{t,k}; \xi_{ij})$, and performs gradient clipping and Gaussian noise addition to satisfy DP:

$$\bar{g}_{ij} = g_{ij} / \max(1, \|g_{ij}\|_2 / C), \quad (2)$$

$$\tilde{g}_i^{t,k} \leftarrow \frac{1}{sR} \sum_{j \in \mathcal{D}_i^k} \bar{g}_{ij} + \frac{C}{sR} \mathcal{N}(0, \sigma^2 C^2 I), \quad (3)$$

where C is the clipping threshold, σ is the noise factor. After K local steps, the server updates the global model θ^{t+1} by adding the averaged aggregate local update to θ^t .

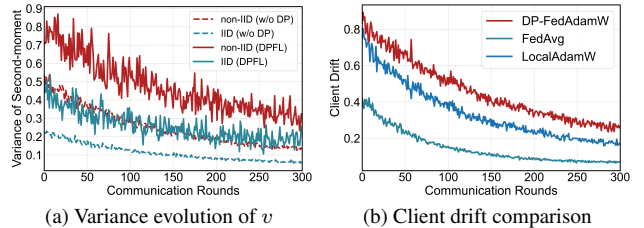


Figure 3. Training on CIFAR-100, Swin-Tiny, $\sigma=1$, $\alpha=0.1$. (a) Non-IID (DPFL) causes high variance in second-moment estimator across clients of DP-LocalAdamW. (b) DP-LocalAdamW suffers from more severe client drift than FedAvg and LocalAdamW.

4. Motivation and challenges

Prior work [48, 78] shows that AdamW can substantially improve convergence and generalization. However, our key observation is that, in DPFL, AdamW fails to exhibit its typical advantages. In fact, in transformer-based models, AdamW sometimes performs worse than SGD, indicating the benefits of AdamW are diminished when privacy constraints and the FL setup introduce additional complexities.

Challenge 1: Variance amplification of the second-moment estimator under non-IID and DP. In FL, non-IID data disperses client gradients, while DP noise further increases the variance of noisy gradients. This high variance accumulates in AdamW’s exponentially weighted moving averages of the first-moment \mathbf{m} and second-moment \mathbf{v} :

$$\begin{aligned} \mathbf{m}_i^{t,k} &\leftarrow \beta_1 \mathbf{m}_i^{t,k-1} + (1 - \beta_1) \tilde{\mathbf{g}}_i^{t,k}, \\ \mathbf{v}_i^{t,k} &\leftarrow \beta_2 \mathbf{v}_i^{t,k-1} + (1 - \beta_2) \tilde{\mathbf{g}}_i^{t,k} \odot \tilde{\mathbf{g}}_i^{t,k}, \end{aligned} \quad (4)$$

where $\beta_1=0.9$, $\beta_2=0.999$ are the exponential decay rates. \odot represents the elementwise (Hadamard) product.

$$\text{Var}(\mathbf{v}^t) \approx \frac{(1 - \beta_2)^2}{1 - \beta_2^2} \text{Var}(\tilde{\mathbf{g}}^t \odot \tilde{\mathbf{g}}^t). \quad (5)$$

Since $\tilde{\mathbf{g}}^t \odot \tilde{\mathbf{g}}^t$ magnifies noise and $\beta_2 \approx 1$ induces slow averaging, the variance of \mathbf{v} grows rapidly and dominates the optimization noise under DP and heterogeneity. Figure 3(a) shows the variance of \mathbf{v} under non-IID+DP remains higher and converges much slower than in IID or non-DP cases.

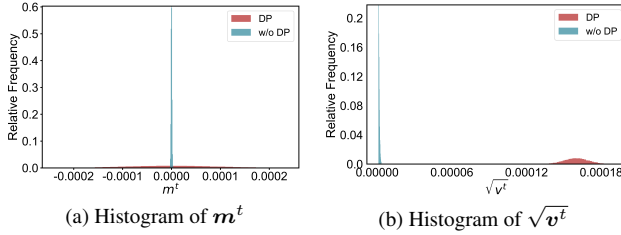


Figure 4. Histogram for DP-LocalAdamW, CIFAR-10, Swin-Tiny, $\sigma=1$, $\alpha=0.1$. (a) The distribution centers of \mathbf{m}^t are aligned with or without DP, but the variance is larger with DP. (b) The distribution of $\sqrt{\mathbf{v}^t}$ shows a significant difference, with the center of the distribution shifting approximately by $\sqrt{\sigma^2 C^2 / (sR)^2}$.

Challenge 2: Systematic bias in the second-moment estimator introduced by DP. Under DP clipping and noise, directly using the perturbed gradient to estimate the second moment produces a systematic bias. This bias is additive and distinct from the initialization bias addressed by Adam’s exponential moving average, so that correction does not remove it in Figure 4. Recall the definition of $\mathbf{v}_i^{t,k}$ from Eq. 4, Eq. 2, Eq. 3, we have

$$\begin{aligned} \mathbb{E}[\tilde{\mathbf{g}}_i^{t,k} \odot \tilde{\mathbf{g}}_i^{t,k}] &= \mathbb{E}[\bar{\mathbf{g}}_i^{t,k} \odot \bar{\mathbf{g}}_i^{t,k}] + \sigma^2 C^2 / (sR)^2 I, \\ \mathbb{E}[\mathbf{v}_i^{t,k}] &= \mathbb{E}[\mathbf{v}_i^{t,k}]_{\text{w/o DP}} + (1 - \beta_2^k) \sigma^2 C^2 / (sR)^2 I. \end{aligned} \quad (6)$$

Challenge 3: Client drift caused by local adaptivity and DP mechanism. In FL, each client optimizes its local objective $f(\cdot)$, creating a gap between local and global optima. AdamW accelerates this by pushing clients toward their local optima, increasing client drift. In DPFL, gradient clipping and noise injection reduce effective sample sizes, making updates noisier and amplifying overfitting. This exacerbates client drift, hindering global model convergence. Figure 3(b) shows that DP-FedAdamW results in higher client

Algorithm 1 DP-FedAdamW

```

1: Initial initial model  $\theta^0$ ; rounds  $T$ ; local steps  $K$ ; step
   size  $\eta$ ; weight decay  $\lambda$ ; AdamW  $(\beta_1, \beta_2, \epsilon)$ ; clip norm
    $C$ ; noise multiplier  $\sigma$ ;  $S$  clients per round
2: for  $t = 1$  to  $T$  do
3:   for selected clients  $i = 1, \dots, S$  in parallel do
4:      $\theta_i^{t,0} \leftarrow \theta^t$ ;  $\mathbf{m}_i^{t,0} \leftarrow \mathbf{0}$ ;  $\mathbf{v}_i^{t,0} \leftarrow \bar{\mathbf{v}}^t$ 
5:     for  $k = 1$  to  $K$  do
6:       sample  $\mathcal{D}_i^k \subset \mathcal{D}_i$  of size  $\lfloor sR \rfloor$ 
7:       for each sample  $j \in \mathcal{D}_i^k$  do
8:          $g_{ij} \leftarrow \nabla f_i(\theta_i^{t,k}; \xi_{ij})$ 
9:          $\bar{g}_{ij} \leftarrow g_{ij} / \max(1, \|g_{ij}\|/C)$ 
10:      end for
11:       $\bar{\mathbf{g}}_i^{t,k} \leftarrow \frac{1}{sR} \sum_{j \in \mathcal{D}_i^k} \bar{g}_{ij} + \frac{C}{sR} \mathcal{N}(0, \sigma^2 C^2 I)$ 
12:       $\mathbf{m}_i^{t,k} \leftarrow \beta_1 \mathbf{m}_i^{t,k-1} + (1 - \beta_1) \bar{\mathbf{g}}_i^{t,k}$ 
13:       $\mathbf{v}_i^{t,k} \leftarrow \beta_2 \mathbf{v}_i^{t,k-1} + (1 - \beta_2) \bar{\mathbf{g}}_i^{t,k} \odot \bar{\mathbf{g}}_i^{t,k}$ 
14:       $\hat{\mathbf{m}}_i^{t,k} \leftarrow \mathbf{m}_i^{t,k} / (1 - \beta_1^k)$ 
15:       $\hat{\mathbf{v}}_i^{t,k} \leftarrow \mathbf{v}_i^{t,k} / (1 - \beta_2^k)$ 
16:       $\vartheta_i^{t,k} \leftarrow 1 / (\sqrt{\hat{\mathbf{v}}_i^{t,k} - (\frac{\sigma C}{sR})^2} + \epsilon)$ 
17:       $\theta_i^{t,k+1} \leftarrow \theta_i^{t,k} - \eta(\hat{\mathbf{m}}_i^{t,k} \odot \vartheta_i^{t,k} + \gamma \Delta_G^t - \lambda \theta_i^{t,k})$ 
18:    end for
19:    Send  $(\theta_i^{t,K} - \theta_i^{t,0}, \bar{\mathbf{v}}_i = \text{Block\_mean}(\mathbf{v}_i^{t,K}))$ 
20:  end for
21:   $\Delta_G^{t+1} = \frac{-1}{SK\eta} \sum_{i=1}^S (\theta_i^{t,K} - \theta_i^{t,0})$ 
22:   $\theta^{t+1} = \theta^t + \frac{1}{S} \sum_{i=1}^S (\theta_i^{t,K} - \theta_i^{t,0})$ 
23:   $\bar{\mathbf{v}}^{t+1} = \frac{1}{S} \sum_{i=1}^S \bar{\mathbf{v}}_i$ 
24:  Broadcast  $(\theta^{t+1}, \bar{\mathbf{v}}^{t+1}, \Delta_G^{t+1})$  to clients
25: end for

```

drift compared to FedAvg and LocalAdamW, where LocalAdamW refers to Federated AdamW without DP.

5. Methodology

To restore the effectiveness of AdamW in DPFL, we propose Differentially Private Federated AdamW (DP-FedAdamW). DP-FedAdamW is built upon a unified perspective: *the moment statistics of AdamW become distorted under non-IID data and DP*. Our design corrects this distortion along three complementary axes: parameter-block aggregation to stabilize second-moment variance, explicit removal of DP-induced bias in the second moment, and local-global update alignment to reduce client drift.

5.1. Second-moment aggregation

To address **Challenge 1**, we stabilize the training process by aggregating the second-moment estimates of AdamW. However, directly aggregating per-parameter second mo-

ments requires communicating an additional vector with the same dimensionality as the model parameters, which almost doubles the communication overhead. We therefore introduce a block-wise aggregation scheme that communicates only *one* statistic per parameter block.

We adopt a parameter-block averaging strategy, where each block shares a single learning rate to capture local curvature effectively. Based on this idea, we partition the parameters into B blocks and compute the `mean` of second-moments within each block (line 19 in Algorithm 1):

$$\bar{v}_b = \frac{1}{|v_b|} \sum_{i \in v_b} v_i, \quad b = 1, \dots, B. \quad (7)$$

Block-wise averaging strategy. We design the blocks to align with the model architecture. The attention-related parameters are partitioned at the granularity of attention heads, while the remaining modules are partitioned at the granularity of whole layers. For each parameter block, we compute the `mean` of its second-moment estimates and transmit only this block-wise statistic:

- **Head-wise Q, K, V.** According to the number of attention heads in the model, each head-specific slice of the `query` (Q), `key` (K), and `value` (V) weight matrix is treated as an independent parameter block. For every such Q/K/V block, we compute and transmit the `mean` of its second-moment estimates.
- **attn.proj and MLP layers.** Each attention output projection layer (`attn.proj`) and each MLP layer is regarded as a single parameter block. For each layer, we aggregate the second-moment estimates of all parameters within the layer and transmit the block-wise `mean`.
- **Embedding and output layers.** Similarly, each Embedding layer and each output (e.g., classification) layer is treated as one parameter block. For these blocks, we also compute and transmit the `mean` of the corresponding second-moment estimates.

CNNs (e.g., ResNet): For convolutional networks, we define each convolutional layer or residual block as one parameter block. This reduces the communication cost from per-parameter second moments to B block-level values while preserving adaptive behavior across different components of the network.

5.2. Unbiased second-moment correction

To address **Challenge 2**, we propose a Bias-Corrected (BC). The correction term subtracts the variance contribution of the noise from the second-moment estimate of DP-AdamW, restoring the scaling behavior of non-private Adam and removing the influence of DP on the second-moment estimation. The update rule is given by (line 16 in Algorithm 1):

$$\vartheta_i^{t,k} = 1 / \left(\sqrt{\hat{v}_i^{t,k} - \left(\frac{\sigma C}{sR} \right)^2} + \epsilon \right) \quad (8)$$

Here, $\hat{v}_i^{t,k}$ denotes the exponential moving average of the (noisy) second moment of the gradient for parameter i , σ is the noise multiplier, C is the clipping norm, and sR is the batch size. The term $\frac{\sigma C}{sR}$ corresponds to the variance of the Gaussian noise added for differential privacy, and subtracting it removes the constant bias introduced by DP noise in the second-moment estimate.

5.3. Local-global alignment

To mitigate **Challenge 3** (client drift under non-IID data with DP), we augment the local AdamW update with an explicit alignment toward the global descent direction. Concretely, we modify the local update rule (line 17 in Algorithm 1) as

$$\theta_i^{t,k+1} = \theta_i^{t,k} - \eta \left(\hat{m}_i^{t,k} \odot \vartheta_i^{t,k} - \lambda \theta_i^{t,k} + \gamma \Delta_G^t \right), \quad (9)$$

where $\Delta_G^t = \frac{-1}{SK\eta} \sum_{i=1}^S (\theta_i^{t,K} - \theta_i^{t,0})$ is an empirical estimate of the global update over S participating clients.

Under non-IID data, the adaptive local gradient $\hat{m}_i^{t,k} \odot \vartheta_i^{t,k}$ is biased toward each client’s own objective. DP clipping distorts the magnitude and direction of these gradients, and DP noise adds high-variance perturbations, pushing the local parameters $\theta_i^{t,k}$ toward different client-specific optima and amplifying the client drift identified in **Challenge 3**. The alignment term $\gamma \Delta_G^t$ softly regularizes each local step toward the global descent direction. It is nearly inactive when a client’s update already follows the global trend, but when non-IID data and DP operations drive the local direction away, the alignment term counteracts this deviation and steers the trajectory back toward the global path. As illustrated in Figure 2, this local–global alignment tightens the spread of client models, reduces cross-client update variance at aggregation, and yields a smoother, more stable global optimization trajectory under strong non-IID and DP.

6. Theoretical analysis

6.1. Convergence analysis

In this part, we give the convergence theoretical analysis of our proposed DP-FedAdamW algorithm. Firstly, we give some standard assumptions for the non-convex function f .

Assumption 1 (Smoothness). (*Smoothness*) The non-convex f_i is a L -smooth function for all $i \in [m]$, i.e., $\|\nabla f_i(\theta_1) - \nabla f_i(\theta_2)\| \leq L \|\theta_1 - \theta_2\|$, for all $\theta_1, \theta_2 \in \mathbb{R}^d$.

Assumption 2 (Bounded Stochastic Gradient). $g_i^t = \nabla f_i(\theta_i^t, \xi_i^t)$ computed by using a sampled mini-batch data ξ_i^t in the local client i is an unbiased estimator of ∇f_i with bounded variance, i.e., $\mathbb{E}_{\xi_i^t} [g_i^t] = \nabla f_i(\theta_i^t)$ and $\mathbb{E}_{\xi_i^t} \|g_i^t - \nabla f_i(\theta_i^t)\|^2 \leq \sigma_i^2$, for all $\theta_i^t \in \mathbb{R}^d$.

Assumption 3 (Bounded Stochastic Gradient II). Each element of stochastic gradient g_i^t is bounded, i.e., $\|g_i^t\|_\infty =$

$\|f_i(\theta_i^t, \xi_i^t)\|_\infty \leq G_g$, for all $\theta_i^t \in \mathbb{R}^d$ and any sampled mini-batch data ξ_i^t .

Theorem 1 (Convergence for non-convex functions). *Under Assumptions A.1, A.2, and A.3, if we take $g^0 = 0$, then DP-FedAdamW converges as follows*

$$\frac{1}{T} \sum_{t=0}^{T-1} \mathbb{E}[\|\nabla f(\theta^t)\|^2] \lesssim \mathcal{O}\left(\sqrt{\frac{L\Delta\sigma_l^2}{SKT\epsilon^2}} + \frac{L\Delta}{T} + \frac{\sigma^2 G_g^2}{s^2 R^2}\right). \quad (10)$$

Here $G_0 := \frac{1}{N} \sum_{i=1}^N \|\nabla f_i(\theta^0)\|^2$, $\Delta = f(\theta^0) - f^*$, S is the number of participating clients per round, σ is DP noise level, σ_l is noise of stochastic gradient, K is the number of local iterations, and T is the total number of communication rounds.

The proof is provided in Appendix 11.1. The convergence rate of DP-FedAdamW is faster than that of DP-LocalAdamW's $\mathcal{O}\left(\sqrt{\frac{L\Delta(\sigma_l^2 + \sigma_g^2)}{SKT\epsilon^2}} + \frac{L\Delta}{T} + \frac{\sigma^2 G_g^2}{s^2 R^2}\right)$, and we do not need bounded heterogeneity assumption. This is due to the suppression of local drift by the global update estimation Δ_G^t . Unlike prior adaptive FL optimizers [65] which rely on heterogeneity assumption, our convergence result holds without such restrictions, making it more widely applicable.

6.2. Privacy analysis

Differential privacy (DP) [11] provides a formal framework for quantifying disclosure risk. We conduct privacy accounting under Rényi DP (RDP) [51], which gives tight bounds under composition and subsampling. Following [52], we finally convert RDP to (ϵ, δ) -DP [51].

Definition 1. (Sample-level DP, [22]). *For any two neighboring datasets \mathcal{D} and \mathcal{D}' that differ in a single sample or record (either by addition or removal), a randomized mechanism $\mathcal{M} : \mathcal{X}^n \rightarrow \mathcal{Y}$ satisfies (ϵ, δ) -DP at the sample level if, for every possible output set $O \subseteq \mathcal{Y}$, the following holds:*

$$\Pr[\mathcal{M}(\mathcal{D}) \in O] \leq e^\epsilon \Pr[\mathcal{M}(\mathcal{D}') \in O] + \delta, \quad (11)$$

where ϵ is the privacy budget, δ is the failure probability.

Definition 2. (Rényi DP, [51]). *For any order $\zeta \in (1, \infty)$, \mathcal{M} satisfies (ζ, ϵ_T) -RDP if for any two neighboring datasets \mathcal{D} , \mathcal{D}' that differ by a single sample, it has:*

$$D_\zeta[\mathcal{M}(\mathcal{D}) \|\mathcal{M}(\mathcal{D}')]:= \frac{1}{\zeta-1} \log \mathbb{E} \left[\left(\frac{p_{\mathcal{M}(\mathcal{D})}(Y)}{p_{\mathcal{M}(\mathcal{D}')}(Y)} \right)^\zeta \right] \leq \epsilon_T, \quad (12)$$

The expectation \mathbb{E} is taken over the output $Y \sim \mathcal{M}(\mathcal{D}')$.

We adopt standard RDP accounting following [52], the cumulative privacy over K local steps and T rounds is:

Theorem 2 (Privacy guarantee). *For DP-FedAdamW, θ^T is (ϵ, δ) -DP towards a third party*

$$\epsilon = \mathcal{O}\left(\frac{s\sqrt{TK \log(2/\delta) \log(2T/\delta)}}{\sigma}\right), \quad (13)$$

Towards the server, accumulative (ϵ_s, δ_s) -DP is

$$\epsilon_s = \epsilon \sqrt{\frac{N}{l}}, \delta_s = \frac{\delta}{2} \left(\frac{1}{l} + 1\right), \quad (14)$$

where N is the number of clients, l is clients sample rate, and s is client data sample rate.

7. Experiments

7.1. Experimental setup

DPFL Algorithms. We conduct experiments on six DPFL algorithms: DP-FedAvg [52], DP-SCAFFOLD [52], DP-FedAvg-LS [34], DP-FedSAM [62], DP-LocalAdamW, and our DP-FedAdamW. In all performance evaluation experiments, the DP noise multiplier σ is fixed. Under the same clipping norm and communication rounds, DP-FedSAM requires roughly twice the privacy budget of other methods, as it injects independent DP noise into two gradient evaluations at each local step. All methods are implemented using PyTorch and executed on NVIDIA RTX 4090 GPUs.

Datasets and data partition. We evaluate DP-FedAdamW on seven datasets covering both vision and language tasks. For image classification, we adopt CIFAR-10, CIFAR-100 [28], and Tiny-ImageNet [30]. For natural language understanding, we consider four GLUE [67] benchmarks: SST-2, QQP, QNLI, and MNLI. We simulate non-IID client data using a Dirichlet partition [25], where each client's distribution is sampled from $\text{Dir}(\alpha)$ with $\alpha \in \{0.1, 0.6, 0.8\}$.

Model architectures. We study three representative architecture families. (1) convolutional neural networks(CNNs): GNResNet-18 evaluated on CIFAR-10/100. (2) vision transformers: ViT-Base for CIFAR-10/100 and Swin-Tiny/Base for CIFAR-10/100 and Tiny-ImageNet. (3) language transformer: RoBERTa-Base assessed on the GLUE.

Configurations. For DP-FedAvg, DP-SCAFFOLD, DP-FedAvg-LS, and DP-FedSAM, the learning rate η is selected from $\{10^{-2}, 3 \times 10^{-2}, 5 \times 10^{-2}, 10^{-1}, 3 \times 10^{-1}\}$ with a weight decay of 0.001. For DP-LocalAdamW, DP-FedAdamW, η is selected from $\{10^{-4}, 3 \times 10^{-4}, 5 \times 10^{-4}, 8 \times 10^{-4}, 10^{-3}\}$ with weight decay 0.01 or 0.001, $\beta_1 = 0.9$, $\beta_2 = 0.999$. We apply cosine learning rate decay, and set DP-FedAdamW to $\gamma=0.5$, weight decay $\lambda=0.01$. For ResNet-18, rounds $T=300$, batch size 50, local step $K=50$. For Transformers, rounds $T=100$, batch size 16, local step $K=20$. The noise multiplier is $\sigma=1$. The privacy failure probability is set to $\delta = 10^{-5}$ for CIFAR10/100 and $\delta = 10^{-6}$ for Tiny-ImageNet. Please refer to Appendix 9.4 for more details of the experimental settings. All results are averaged over 5 runs with std reported.

Table 2. Averaged test accuracy (%) and privacy budget comparison on CIFAR-10 and CIFAR-100 using ResNet-18 and ViT-Base. Assuming DP-FedAvg is (ϵ, δ) -DP, all other methods share this budget except DP-FedSAM, which is approximately $(2\epsilon, \delta)$ -DP.

Method	CIFAR-10 (ResNet-18)		CIFAR-100 (ResNet-18)		CIFAR-10 (ViT-Base)		CIFAR-100 (ViT-Base)		Privacy Budget
	$\alpha=0.6$	$\alpha=0.1$	$\alpha=0.6$	$\alpha=0.1$	$\alpha=0.6$	$\alpha=0.1$	$\alpha=0.6$	$\alpha=0.1$	
DP-FedAvg	71.69 \pm 0.37	60.38 \pm 0.21	31.13 \pm 0.57	25.04 \pm 0.72	90.51 \pm 0.37	78.85 \pm 0.21	45.86 \pm 0.57	13.41 \pm 0.72	(ϵ, δ)
DP-SCAFFOLD	71.79 \pm 0.44	59.04 \pm 0.39	31.52 \pm 0.36	24.94 \pm 0.58	90.88 \pm 0.52	80.69 \pm 0.64	62.45 \pm 0.57	64.69 \pm 0.76	(ϵ, δ)
DP-FedAvg-LS	72.27 \pm 0.57	60.84 \pm 0.45	35.91 \pm 0.54	28.68 \pm 0.52	91.48 \pm 0.47	88.48 \pm 0.50	67.76 \pm 0.58	65.85 \pm 0.63	(ϵ, δ)
DP-FedSAM	67.39 \pm 0.41	57.04 \pm 0.46	30.36 \pm 0.50	24.03 \pm 0.66	91.76 \pm 0.55	89.35 \pm 0.65	70.24 \pm 0.63	66.27 \pm 0.65	$(2\epsilon, \delta)$
DP-LocalAdamW	71.73 \pm 0.47	60.55 \pm 0.53	34.92 \pm 0.69	28.70 \pm 0.81	91.16 \pm 0.47	89.85 \pm 0.53	68.21 \pm 0.69	65.24 \pm 0.81	(ϵ, δ)
DP-FedAdamW	74.81\pm0.19	64.65\pm0.24	39.56\pm0.42	33.55\pm0.50	92.02\pm0.49	90.30\pm0.24	71.59\pm0.42	67.56\pm0.50	(ϵ, δ)

Table 3. Averaged test accuracy (%) and privacy budget comparison on CIFAR-100 and Tiny-ImageNet using Swin-Tiny and Swin-Base.

Method	CIFAR-100 (Swin-T)		CIFAR-100 (Swin-B)		Tiny-ImageNet (Swin-T)		Tiny-ImageNet (Swin-B)		Privacy Budget
	$\alpha=0.6$	$\alpha=0.1$	$\alpha=0.6$	$\alpha=0.1$	$\alpha=0.6$	$\alpha=0.1$	$\alpha=0.6$	$\alpha=0.1$	
DP-FedAvg	36.96 \pm 0.50	28.07 \pm 0.31	65.61 \pm 0.27	60.77 \pm 0.32	18.82 \pm 0.94	10.12 \pm 1.36	52.04 \pm 0.66	36.19 \pm 0.74	(ϵ, δ)
DP-SCAFFOLD	41.68 \pm 0.64	33.52 \pm 0.65	68.03 \pm 0.55	65.34 \pm 0.49	21.91 \pm 0.78	14.54 \pm 0.72	53.78 \pm 0.79	43.55 \pm 0.60	(ϵ, δ)
DP-FedAvg-LS	41.95 \pm 0.53	36.72 \pm 0.65	68.80 \pm 0.52	66.08 \pm 0.56	23.03 \pm 0.64	15.99 \pm 0.68	55.83 \pm 0.66	47.46 \pm 0.57	(ϵ, δ)
DP-FedSAM	44.19 \pm 0.48	38.43 \pm 0.62	70.44 \pm 0.57	66.28 \pm 0.64	22.75 \pm 0.65	16.86 \pm 0.77	56.12 \pm 0.74	48.08 \pm 0.62	$(2\epsilon, \delta)$
DP-LocalAdamW	42.04 \pm 0.63	35.51 \pm 0.58	68.33 \pm 0.33	65.28 \pm 0.39	23.41 \pm 0.87	15.81 \pm 0.73	54.58 \pm 0.60	46.52 \pm 0.64	(ϵ, δ)
DP-FedAdamW	46.77\pm0.38	39.36\pm0.55	71.58\pm0.30	67.45\pm0.26	23.96\pm0.50	19.19\pm0.55	58.44\pm0.54	50.76\pm0.51	(ϵ, δ)

Table 4. Averaged test accuracy (%) on RoBERTa-Base.

Method	SST-2	QQP	QNLI	MNLI
DP-FedAvg	49.08 \pm 0.12	63.18 \pm 0.50	49.46 \pm 0.44	35.45 \pm 0.20
DP-SCAFFOLD	52.35 \pm 0.18	66.87 \pm 0.42	52.62 \pm 0.52	38.74 \pm 0.32
DP-FedAvg-LS	68.38 \pm 0.50	72.59 \pm 0.48	69.22 \pm 0.68	50.46 \pm 0.55
DP-FedSAM	70.95 \pm 0.62	75.66 \pm 0.53	70.54 \pm 0.63	56.88 \pm 0.56
DP-LocalAdamW	91.04 \pm 0.53	82.33 \pm 0.59	86.07 \pm 0.47	75.20 \pm 0.44
DP-FedAdamW	91.17\pm0.32	83.34\pm0.39	86.33\pm0.34	78.68\pm0.38

7.2. Performance on vision datasets

ResNet-18 on CIFAR-10/100. Table 2 summarizes the results on CIFAR-10/100 under different heterogeneity levels ($\alpha=0.6$ and $\alpha=0.1$). DP-FedAdamW achieves the best performance across all settings, reaching 74.81% and 64.65% on CIFAR-10, and 39.56% and 33.55% on CIFAR-100. When the data heterogeneity is severe ($\alpha=0.1$), DP-FedAdamW surpasses the SOTA baselines (DP-FedAvg-LS for CIFAR-10 and DP-LocalAdamW for CIFAR-100) by 3.81% and 4.85%, respectively.

ViT-Base on CIFAR-10/100. We fine-tune ViT-Base on CIFAR-10/100, and the results are reported in Table 2 under $\alpha=0.6$ and $\alpha=0.1$. DP-FedAdamW consistently achieves the best performance. On CIFAR-100 with $\alpha=0.1$, it outperforms the strongest baseline DP-FedSAM by 1.29%. Recall that, under our DP configuration, DP-FedSAM is trained with a much weaker privacy guarantee (it uses twice the privacy budget of the other methods).

Swin-Tiny/Base on CIFAR-10/100/Tiny-ImageNet. We fine-tune Swin-Tiny and Swin-Base on CIFAR-10, CIFAR-100, and Tiny-ImageNet, and report the results in Tables 3, 10. DP-FedAdamW consistently attains the highest

accuracy across all settings. For example, on CIFAR-100 with Swin-Tiny at $\alpha=0.6$, it reaches 46.77%, outperforming the strongest baseline DP-FedSAM by 2.58%. On Tiny-ImageNet with Swin-Base at $\alpha=0.1$, it achieves 50.85%, exceeding DP-FedSAM by 2.77%. Figure 5 (c,d) shows that DP-FedAdamW achieves advantage on Swin-Tiny.

7.3. Performance on language datasets

RoBERTa-Base on GLUE. We further evaluate our method on four GLUE tasks (SST-2, QQP, QNLI, MNLI) by fine-tuning RoBERTa-Base under $\alpha=0.8$, and report the results in Table 4. DP-FedAdamW attains the best accuracy on all tasks, reaching 91.17%, 83.34%, 86.33%, and 78.68%, respectively. On the MNLI, DP-FedAdamW outperforms the baseline DP-LocalAdamW by 3.48%, showing that the benefits of DP-FedAdamW extend from vision benchmarks to language understanding in the DPFL setting.

7.4. Discussion for DP with AdamW in FL

Performance under different privacy budgets ϵ . Table 5 reports the results of Swin-Base on CIFAR-10, CIFAR-100, and Tiny-ImageNet under $\epsilon=1, 2, 3$ with $\alpha=0.1$. As expected, all methods benefit from larger ϵ (weaker privacy). Notably, the performance gap between DP-FedAdamW and other methods is most pronounced when ϵ is small, i.e., under stronger privacy constraints. For instance, on CIFAR-10, DP-FedAdamW achieves 77.50% at $\epsilon=1$, surpassing the best baseline by 5.93%. These results show that DP-FedAdamW achieves a superior utility-privacy trade-off.

Noise multiplier σ . Results are provided in Appendix 9.1.

Table 5. Effect of privacy budgets (ϵ) on test accuracy (%) using Swin-Base, $\alpha = 0.1$.

Method	CIFAR-10			CIFAR-100			Tiny-ImageNet		
	$\epsilon=1$	$\epsilon=2$	$\epsilon=3$	$\epsilon=1$	$\epsilon=2$	$\epsilon=3$	$\epsilon=1$	$\epsilon=2$	$\epsilon=3$
DP-FedAvg	66.52 \pm 0.89	72.63 \pm 0.55	88.02 \pm 0.76	19.66 \pm 1.52	42.98 \pm 0.60	57.73 \pm 0.55	20.65 \pm 0.77	37.48 \pm 0.54	45.32 \pm 0.47
DP-SCAFFOLD	66.39 \pm 0.68	72.81 \pm 0.53	88.07 \pm 0.66	22.38 \pm 0.67	44.52 \pm 0.68	59.85 \pm 0.52	20.93 \pm 0.66	38.40 \pm 0.51	47.06 \pm 0.30
DP-FedAvg-LS	71.57 \pm 1.02	75.02 \pm 0.59	88.96 \pm 0.54	25.77 \pm 0.61	49.54 \pm 0.59	62.46 \pm 0.53	26.89 \pm 0.46	46.57 \pm 0.44	48.83 \pm 0.21
DP-FedSAM	53.51 \pm 1.39	59.33 \pm 0.86	76.82 \pm 0.97	12.33 \pm 0.64	28.32 \pm 0.49	46.93 \pm 0.50	10.88 \pm 0.95	26.76 \pm 0.78	41.69 \pm 0.45
DP-LocalAdamW	66.57 \pm 1.35	73.04 \pm 0.58	88.83 \pm 0.71	24.69 \pm 0.88	47.26 \pm 0.59	62.18 \pm 0.61	28.40 \pm 0.72	46.62 \pm 0.37	48.55 \pm 0.28
DP-FedAdamW	77.50\pm0.54	80.37\pm0.58	89.98\pm0.55	30.06\pm0.41	52.11\pm0.54	65.47\pm0.42	34.23\pm0.50	50.95\pm0.26	52.53\pm0.22

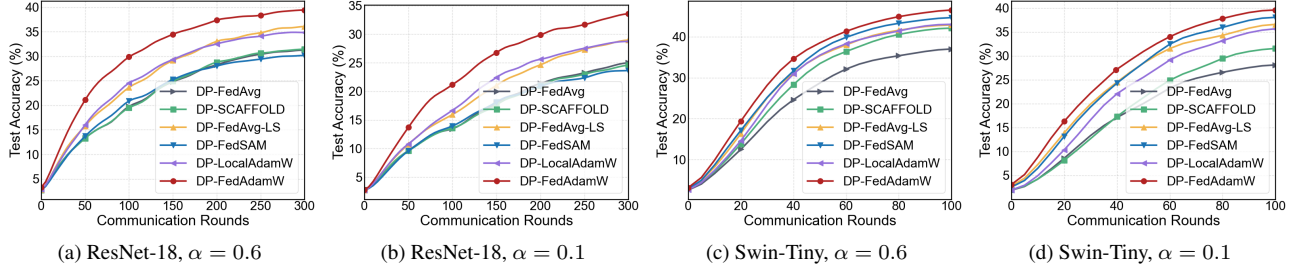


Figure 5. Test accuracy (%) on CIFAR-100 using ResNet-18 and Swin-Tiny under the Dirichlet $\alpha = 0.6$ and $\alpha = 0.1$ settings.

Table 6. Ablation on the main components of DP-FedAdamW on Swin-Base. We report test accuracy (%) on CIFAR-100 and Tiny-ImageNet under non-IID setting ($\alpha = 0.1$). ‘‘Agg’’ denotes block-wise second-moment aggregation, ‘‘BC’’ the DP bias correction, and ‘‘Align’’ the local–global alignment term.

Method	CIFAR-100	Tiny-ImageNet
DP-LocalAdamW	65.28	46.52
w/o Agg	66.41	47.35
w/o BC	67.02	48.11
w/o Align	66.37	47.82
DP-FedAdamW (full)	67.42	50.73

Table 7. Ablation study of moment aggregation strategies of DP-LocalAdamW on CIFAR-100 with Swin-Base under $\alpha=0.1$.

Strategy	CIFAR-100	Tiny-ImageNet	Comm(\uparrow)
NoAgg	66.21 \pm 0.11	49.12 \pm 0.12	5.7M
Agg- v	67.52 \pm 0.12	50.88 \pm 0.12	11.4M
Agg-mean- v	67.45\pm0.10	50.76\pm0.10	5.7M

Table 8. Impact of γ using Swin-Base ($\alpha=0.1$).

γ	0.00	0.25	0.50	0.75	1.00
CIFAR-100 (%)	66.37	67.01	67.45	67.10	66.52
Tiny-ImageNet (%)	47.82	49.36	50.76	50.21	49.18

7.5. Ablation study

Effect of each component. DP-FedAdamW differs from DP-LocalAdamW in three aspects: (i) block-wise second-moment aggregation (Agg); (ii) DP bias correction on the second-moment (BC); (iii) local–global alignment term (Align). We construct several variants by removing one

Table 9. Comparison with DP variants of federated adaptive optimizers under the same DP settings (Swin-Base, $\alpha=0.1$, $\sigma=1$).

Method	CIFAR-100	Tiny-ImageNet
DP-FedOpt(Adam) [59]	64.54 \pm 0.56	44.81 \pm 0.62
DP-FAFED [69]	65.75 \pm 0.54	46.10 \pm 0.67
DP-FedLADA [65]	66.03 \pm 0.61	47.85 \pm 0.57
DP-FedAdamW (ours)	67.45\pm0.26	50.76\pm0.51

component at a time, while keeping all other settings fixed.

Table 9 shows that each component yields a gain, and their combination achieves the best performance. Bias correction (BC) improves robustness to DP noise, the local–global alignment stabilizes optimization under non-IID and DP, and block-wise aggregation provides an additional improvement with negligible communication overhead.

Impact of aggregation strategy. Table 7 shows that our block-wise averaging strategy, Agg-mean- v , achieves the best balance between accuracy and communication cost. Agg-mean- v achieves comparable gains with only $\mathcal{O}(B)$ communication, where B is the number of blocks, demonstrating its scalability and ability to stabilize updates even under strict communication budgets.

Effect of the alignment coefficient γ . Table 8 varies γ on Swin-Base ($\alpha=0.1$). Increasing γ from 0.0 to 0.5 improves accuracy on CIFAR-100 and Tiny-ImageNet, indicating that a moderate alignment term effectively counteracts client drift and stabilizes optimization under DP noise. Further increasing γ beyond 0.5 leads to a slight degradation, as overly strong alignment over-constrains local updates. We therefore set $\gamma=0.5$ as the default.

Comparison with DP variants of federated adaptive

optimizers. As shown in Table 9, on Swin-Base with Dirichlet $\alpha=0.1$, DP noise $\sigma=1$, simply adding DP to existing federated adaptive optimizers yields limited gains. DP-FAFED and DP-FedLADA slightly outperform DP-FedOpt(Adam) on both CIFAR-100 and Tiny-ImageNet. Our DP-FedAdamW consistently achieves the best performance, with roughly 1.42% on CIFAR-100 and 2.91% on Tiny-ImageNet compared to the SOTA DP baseline.

8. Conclusion

In this work, we revisited AdamW for differentially private federated learning and revealed that a naïve adoption leads to amplified second-moment variance, systematic DP-induced bias, and pronounced client drift under small-batch local training. Building on these insights, we introduced DP-FedAdamW, which integrates block-wise second-moment aggregation, explicit DP bias correction, and a local–global alignment mechanism, with non-convex convergence and sample-level privacy guarantees. Experiments on vision (CIFAR-10/100, Tiny-ImageNet with ResNet/ViT/Swin) and language (GLUE with RoBERTa) benchmarks demonstrate DP-FedAdamW consistently surpasses SOTA DPFL baselines under the same privacy budgets, especially in highly non-IID regimes.

References

- [1] Martin Abadi, Andy Chu, Ian Goodfellow, H Brendan McMahan, Ilya Mironov, Kunal Talwar, and Li Zhang. Deep learning with differential privacy. In *Proceedings of the 2016 ACM SIGSAC conference on computer and communications security*, pages 308–318, 2016. 1
- [2] Josh Achiam, Steven Adler, Sandhini Agarwal, Lama Ahmad, Ilge Akkaya, Florencia Leoni Aleman, Diogo Almeida, Janko Altenschmidt, Sam Altman, Shyamal Anadkat, et al. Gpt-4 technical report. *arXiv preprint arXiv:2303.08774*, 2023. 1
- [3] Weixin An, Yingjie Yue, Yuanyuan Liu, Fanhua Shang, and Hongying Liu. A numerical des perspective on unfolded linearized admm networks for inverse problems. In *Proceedings of the 30th ACM International Conference on Multimedia*, pages 5065–5073, 2022. 3
- [4] Weixin An, Yuanyuan Liu, Fanhua Shang, and Hongying Liu. Robust and faster zeroth-order minimax optimization: complexity and applications. *Advances in Neural Information Processing Systems*, 37:37050–37069, 2024.
- [5] Weixin An, Yuanyuan Liu, Fanhua Shang, Hongying Liu, and Licheng Jiao. Des-inspired accelerated unfolded linearized admm networks for inverse problems. *IEEE Transactions on Neural Networks and Learning Systems*, 36(3): 5319–5333, 2024. 3
- [6] Xiangyi Chen, Xiaoyun Li, and Ping Li. Toward communication efficient adaptive gradient method. In *Proceedings of the 2020 ACM-IMS on Foundations of Data Science Conference*, pages 119–128, 2020. 3
- [7] Yuhang Chen, Wenke Huang, and Mang Ye. Fair federated learning under domain skew with local consistency and domain diversity. In *Proceedings of the IEEE/CVF Conference on Computer Vision and Pattern Recognition*, pages 12077–12086, 2024. 1
- [8] Qiao Ding, Nanyu Li, Heng Ding, Jian Wang, Tao Li, Yongqing Chen, Yantuan Xian, and Junyang Chen. Traffic prediction and load balancing routing algorithm based on deep q-network for sd-iot. *Advanced Engineering Informatics*, 68:103596, 2025. 3
- [9] Qiao Ding, Heng Ding, Jian Wang, Yantuan Xian, Tao Li, Nanyu Li, Tao Fang, and Junyang Chen. Enhancing news classification: Domain-specific guided pretraining based on adaptive selective masking. *Knowledge-Based Systems*, page 115516, 2026. 3
- [10] Cynthia Dwork. Differential privacy. In *International colloquium on automata, languages, and programming*, pages 1–12. Springer, 2006. 1
- [11] Cynthia Dwork, Aaron Roth, et al. The algorithmic foundations of differential privacy. *Foundations and Trends® in Theoretical Computer Science*, 9(3–4):211–407, 2014. 6
- [12] Mingyuan Fan, Cen Chen, Chengyu Wang, Xiaodan Li, and Wenmeng Zhou. Refiner: Data refining against gradient leakage attacks in federated learning. In *34th USENIX Security Symposium (USENIX Security 25)*, pages 3005–3024, 2025. 1
- [13] Chen Feng and Ioannis Patras. MaskCon: Masked Contrastive Learning for Coarse-Labelled Dataset. In *Proceed-*

- ings of the *IEEE/CVF Conference on Computer Vision and Pattern Recognition (CVPR)*, 2023. 3
- [14] Chen Feng, Georgios Tzimiropoulos, and Ioannis Patras. SSR: An Efficient and Robust Framework for Learning with Unknown Label Noise. In *33rd British Machine Vision Conference (BMVC)*, 2022.
- [15] Chen Feng, Georgios Tzimiropoulos, and Ioannis Patras. CLIPCleaner: Cleaning Noisy Labels with CLIP. In *The 32nd ACM International Conference on Multimedia (ACM MM)*, 2024.
- [16] Chen Feng, Georgios Tzimiropoulos, and Ioannis Patras. NoiseBox: Towards More Efficient and Effective Learning with Noisy Labels. *IEEE Transactions on Circuits and Systems for Video Technology*, 2024.
- [17] Chen Feng, Ziquan Liu, Zhuo Zhi, Ilija Bogunovic, Carsten Gerner-Beuerle, and Miguel R. D. Rodrigues. PROSAC: Provably safe certification for machine learning models under adversarial attacks. In *The 39th Annual AAAI Conference on Artificial Intelligence (AAAI) [Oral]*, 2025.
- [18] Chen Feng, Nicu Sebe, Georgios Tzimiropoulos, Miguel R. D. Rodrigues, and Ioannis Patras. Unveiling open-set noise: Theoretical insights into label noise. In *The 33rd ACM International Conference on Multimedia (ACM MM)*, 2025.
- [19] Chen Feng, Minghe Shen, Ananth Balashankar, Carsten Gerner-Beuerle, and Miguel R. D. Rodrigues. Noisy but valid: Robust statistical evaluation of LLMs with imperfect judges. In *The Fourteenth International Conference on Learning Representations (ICLR)*, 2026.
- [20] Chen Feng, Zhuo Zhi, Zhao Huang, Jiawei Ge, Ling Xiao, Nicu Sebe, Georgios Tzimiropoulos, and Ioannis Patras. Deconstructing the failure of ideal noise correction: A three-pillar diagnosis. In *Proceedings of the IEEE/CVF Conference on Computer Vision and Pattern Recognition (CVPR)*, 2026. 3
- [21] Pierre Foret, Ariel Kleiner, Hossein Mobahi, and Behnam Neyshabur. Sharpness-aware minimization for efficiently improving generalization. In *ICLR*, 2021. 2
- [22] Jie Fu, Yuan Hong, Xinpeng Ling, Leixia Wang, Xun Ran, Zhiyu Sun, Wendy Hui Wang, Zhili Chen, and Yang Cao. Differentially private federated learning: A systematic review. *arXiv preprint arXiv:2405.08299*, 2024. 1, 6
- [23] Robin C Geyer, Tassilo Klein, and Moin Nabi. Differentially private federated learning: A client level perspective. *arXiv preprint arXiv:1712.07557*, 2017. 1
- [24] Xiaolan Gu, Ming Li, and Li Xiong. {DP-BREM}:{Differentially-Private} and {Byzantine-Robust} federated learning with client momentum. In *34th USENIX Security Symposium (USENIX Security 25)*, pages 3065–3082, 2025. 1
- [25] Tzu-Ming Harry Hsu, Hang Qi, and Matthew Brown. Measuring the effects of non-identical data distribution for federated visual classification. *arXiv preprint arXiv:1909.06335*, 2019. 6
- [26] Jacob Devlin Ming-Wei Chang Kenton, Lee Kristina Toutanova, et al. Bert: Pre-training of deep bidirectional transformers for language understanding. In *Proceedings of naacL-HLT*. Minneapolis, Minnesota, 2019. 1
- [27] Diederik P Kingma. Adam: A method for stochastic optimization. *arXiv preprint arXiv:1412.6980*, 2014. 3
- [28] Alex Krizhevsky. Learning multiple layers of features from tiny images. Technical report, University of Toronto, 2009. Technical Report. 6, 1, 2
- [29] Frederik Kunstner, Alan Milligan, Robin Yadav, Mark Schmidt, and Alberto Bietti. Heavy-tailed class imbalance and why adam outperforms gradient descent on language models. In *Advances in Neural Information Processing Systems*, pages 30106–30148. Curran Associates, Inc., 2024. 3
- [30] Ya Le and Xuan Yang. Tiny imagenet visual recognition challenge, 2015. Stanford CS231N. 6, 1, 2
- [31] Yuqi Li, Kai Li, Xin Yin, Zhifei Yang, Junhao Dong, Zeyu Dong, Chuanguang Yang, Yingli Tian, and Yao Lu. Sep-prune: Structured pruning for efficient deep speech separation. *arXiv preprint arXiv:2505.12079*, 2025. 3
- [32] Yuqi Li, Chuanguang Yang, Hansheng Zeng, Zeyu Dong, Zhulin An, Yongjun Xu, Yingli Tian, and Hao Wu. Frequency-aligned knowledge distillation for lightweight spatiotemporal forecasting. In *Proceedings of the IEEE/CVF International Conference on Computer Vision*, pages 7262–7272, 2025.
- [33] Yuqi Li, Siwei Meng, Chuanguang Yang, Weilun Feng, Junming Liu, Zhulin An, Yikai Wang, and Yingli Tian. A comprehensive survey of interaction techniques in 3d scene generation. *Authorea Preprints*, 2026. 3
- [34] Zhicong Liang, Bao Wang, Quanquan Gu, Stanley Osher, and Yuan Yao. Differentially private federated learning with laplacian smoothing. *Applied and Computational Harmonic Analysis*, 72:101660, 2024. 2, 6
- [35] Bangyan Liao, Zhenjun Zhao, Haoang Li, Yi Zhou, Yingping Zeng, Hao Li, and Peidong Liu. Convex relaxation for robust vanishing point estimation in manhattan world. In *Proceedings of the Computer Vision and Pattern Recognition Conference*, pages 15823–15832, 2025. 3
- [36] Dingyuan Liu, Qiannan Shen, and Jiacy Liu. The health-wealth gradient in labor markets: Integrating health, insurance, and social metrics to predict employment density. *Computation*, 14(1):22, 2026. 3
- [37] Junxu Liu, Jian Lou, Li Xiong, Jinfei Liu, and Xiaofeng Meng. Cross-silo federated learning with record-level personalized differential privacy. In *Proceedings of the 2024 on ACM SIGSAC Conference on Computer and Communications Security*, pages 303–317, 2024. 2
- [38] Junkang Liu, Fanhua Shang, Yuanyuan Liu, Hongying Liu, Yuangang Li, and YunXiang Gong. Fedbcgd: Communication-efficient accelerated block coordinate gradient descent for federated learning. In *Proceedings of the 32nd ACM International Conference on Multimedia*, pages 2955–2963, 2024. 3
- [39] Junkang Liu, Yuanyuan Liu, Fanhua Shang, Hongying Liu, Jin Liu, and Wei Feng. Improving generalization in federated learning with highly heterogeneous data via momentum-based stochastic controlled weight averaging. In *Forty-second International Conference on Machine Learning*, 2025. 3

- [40] Junkang Liu, Fanhua Shang, Yuxuan Tian, Hongying Liu, and Yuanyuan Liu. Consistency of local and global flatness for federated learning. In *Proceedings of the 33rd ACM International Conference on Multimedia*, page 3875–3883, New York, NY, USA, 2025. Association for Computing Machinery. 3
- [41] Junkang Liu, Fanhua Shang, Yuxuan Tian, Hongying Liu, and Yuanyuan Liu. Consistency of local and global flatness for federated learning. In *Proceedings of the 33rd ACM International Conference on Multimedia*, pages 3875–3883, 2025. 3
- [42] Junkang Liu, Fanhua Shang, Junchao Zhou, Hongying Liu, Yuanyuan Liu, and Jin Liu. Fedmuon: Accelerating federated learning with matrix orthogonalization. *arXiv preprint arXiv:2510.27403*, 2025. 3
- [43] Junkang Liu, Fanhua Shang, Kewen Zhu, Hongying Liu, Yuanyuan Liu, and Jin Liu. Fedadamw: A communication-efficient optimizer with convergence and generalization guarantees for federated large models. *arXiv preprint arXiv:2510.27486*, 2025. 3
- [44] Junkang Liu, Yuxuan Tian, Fanhua Shang, Yuanyuan Liu, Hongying Liu, Junchao Zhou, and Daorui Ding. Dp-fedpgn: Finding global flat minima for differentially private federated learning via penalizing gradient norm. *arXiv preprint arXiv:2510.27504*, 2025. 3
- [45] Yuanyuan Liu, Fanhua Shang, Weixin An, Hongying Liu, and Zhouchen Lin. Kill a bird with two stones: Closing the convergence gaps in non-strongly convex optimization by directly accelerated svrg with double compensation and snapshots. In *International Conference on Machine Learning*, pages 14008–14035. PMLR, 2022. 3
- [46] Yuanyuan Liu, Fanhua Shang, Weixin An, Junhao Liu, Hongying Liu, and Zhouchen Lin. A single-loop accelerated extra-gradient difference algorithm with improved complexity bounds for constrained minimax optimization. *Advances in Neural Information Processing Systems*, 36:61699–61711, 2023. 3
- [47] Ze Liu, Yutong Lin, Yue Cao, Han Hu, Yixuan Wei, Zheng Zhang, Stephen Lin, and Baining Guo. Swin transformer: Hierarchical vision transformer using shifted windows. In *Proceedings of the IEEE/CVF international conference on computer vision*, pages 10012–10022, 2021. 1
- [48] Ilya Loshchilov, Frank Hutter, et al. Fixing weight decay regularization in adam. *arXiv preprint arXiv:1711.05101*, 5(5):5, 2017. 1, 3
- [49] Brendan McMahan, Eider Moore, Daniel Ramage, Seth Hampson, and Blaise Aguera y Arcas. Communication-efficient learning of deep networks from decentralized data. In *Artificial intelligence and statistics*, pages 1273–1282. PMLR, 2017. 1
- [50] Lei Meng, Zhuang Qi, Lei Wu, Xiaoyu Du, Zhaochuan Li, Lizhen Cui, and Xiangxu Meng. Improving global generalization and local personalization for federated learning. *IEEE Transactions on Neural Networks and Learning Systems*, 36(1):76–87, 2025. 3
- [51] Ilya Mironov. Rényi differential privacy. In *Proc. IEEE computer security foundations symposium (CSF)*, pages 263–275, 2017. 6
- [52] Maxence Noble, Aurélien Bellet, and Aymeric Dieuleveut. Differentially private federated learning on heterogeneous data. In *International conference on artificial intelligence and statistics*, pages 10110–10145. PMLR, 2022. 1, 2, 6
- [53] Stanley Osher, Bao Wang, Penghang Yin, Xiyang Luo, Farzin Barekat, Minh Pham, and Alex Lin. Laplacian smoothing gradient descent. *Research in the Mathematical Sciences*, 9(3):55, 2022. 2
- [54] Xin Qi, Meixuan Li, Sijin Zhou, Wei Feng, and Zhuang Qi. Federated learning for science: A survey on the path to a trustworthy collaboration ecosystem. *Authorea Preprints*, 2025. 3
- [55] Xin Qi, Tao Xu, Chengrun Dang, Zhuang Qi, Lei Meng, and Han Yu. Federated learning in oncology: bridging artificial intelligence innovation and privacy protection. *Information Fusion*, page 104154, 2026.
- [56] Zhuang Qi, Lei Meng, Zitan Chen, Han Hu, Hui Lin, and Xiangxu Meng. Cross-silo prototypical calibration for federated learning with non-iid data. In *Proceedings of the 31st ACM international conference on multimedia*, pages 3099–3107, 2023. 3
- [57] Sashank J Reddi, Satyen Kale, and Sanjiv Kumar. On the convergence of adam and beyond. In *International Conference on Learning Representations*, 2018. 3
- [58] Sashank J Reddi, Satyen Kale, and Sanjiv Kumar. On the convergence of adam and beyond. *arXiv preprint arXiv:1904.09237*, 2019. 3
- [59] Sashank J Reddi, Zachary Charles, Manzil Zaheer, Zachary Garrett, Keith Rush, Jakub Konečný, Sanjiv Kumar, and Hugh Brendan McMahan. Adaptive federated optimization. In *International Conference on Learning Representations*, 2021. 3, 8
- [60] Qiannan Shen and Jing Zhang. Ai-enhanced disaster risk prediction with explainable shap analysis: A multi-class classification approach using xgboost. 2025. Preprint, Version 1, posted December 31, 2025. 3
- [61] Qiannan Shen and Jing Zhang. Mftformer: Meteorological-frequency-temporal transformer with block-aligned fusion for traffic flow prediction. *Research Square*, 2026. Preprint, doi:10.21203/rs.3.rs-8770196/v1. 3
- [62] Yifan Shi, Yingqi Liu, Kang Wei, Li Shen, Xueqian Wang, and Dacheng Tao. Make landscape flatter in differentially private federated learning. In *Proceedings of the IEEE/CVF conference on computer vision and pattern recognition*, pages 24552–24562, 2023. 2, 6
- [63] Wenxi Sun, Zhichun Qi, and Qiannan Shen. High-recall deep learning: A gated recurrent unit approach to bank account fraud detection on imbalanced data. 2025. 3
- [64] Wenxi Sun, Qiannan Shen, Yijun Gao, Qinkai Mao, Tong-song Qi, and Shuo Xu. Objective over architecture: Fraud detection under extreme imbalance in bank account opening. *Computation*, 13(12):290, 2025. 3
- [65] Yan Sun, Li Shen, Hao Sun, Liang Ding, and Dacheng Tao. Efficient federated learning via local adaptive amended optimizer with linear speedup. *IEEE Transactions on Pattern Analysis and Machine Intelligence*, 45(12):14453–14464, 2023. 3, 6, 8

- [66] Zhonglin Sun, Chen Feng, Ioannis Patras, and Georgios Tzimiropoulos. LAFS: Landmark-based Facial Self-supervised Learning for Face Recognition. In *Proceedings of the IEEE/CVF Conference on Computer Vision and Pattern Recognition (CVPR)*, 2024. 3
- [67] Alex Wang, Amanpreet Singh, Julian Michael, Felix Hill, Omer Levy, and Samuel Bowman. Glue: A multi-task benchmark and analysis platform for natural language understanding. In *Proceedings of the 2018 EMNLP workshop BlackboxNLP: Analyzing and interpreting neural networks for NLP*, pages 353–355, 2018. 6, 1
- [68] Chengkun Wei, Weixian Li, Gong Chen, and Wenzhi Chen. Dc-sgd: Differentially private sgd with dynamic clipping through gradient norm distribution estimation. *IEEE Transactions on Information Forensics and Security*, 2025. 2
- [69] Xidong Wu, Feihu Huang, Zhengmian Hu, and Heng Huang. Faster adaptive federated learning. In *Proceedings of the AAAI conference on artificial intelligence*, pages 10379–10387, 2023. 3, 8
- [70] Shuo Xie and Zhiyuan Li. Implicit bias of adamw: ℓ_∞ -norm constrained optimization. In *International Conference on Machine Learning*, pages 54488–54510. PMLR, 2024. 3
- [71] Runhua Xu, Shiqi Gao, Chao Li, James Joshi, and Jianxin Li. Dual defense: Enhancing privacy and mitigating poisoning attacks in federated learning. *Advances in Neural Information Processing Systems*, 37:70476–70498, 2024. 1
- [72] Xiangrui Xu, Zhize Li, Yufei Han, Bin Wang, Jiqiang Liu, and Wei Wang. From risk to resilience: Towards assessing and mitigating the risk of data reconstruction attacks in federated learning. In *34th USENIX Security Symposium (USENIX Security 25)*, pages 3141–3160, 2025. 1
- [73] Yuchen Yang, Bo Hui, Haolin Yuan, Neil Gong, and Yinzhi Cao. {PrivateFL}: Accurate, differentially private federated learning via personalized data transformation. In *32nd USENIX Security Symposium (USENIX Security 23)*, pages 1595–1612, 2023. 1
- [74] Yushun Zhang, Congliang Chen, Tian Ding, Ziniu Li, Ruoyu Sun, and Zhiquan Luo. Why transformers need adam: A hessian perspective. *Advances in neural information processing systems*, 37:131786–131823, 2024. 3
- [75] Zhenjun Zhao. Balf: Simple and efficient blur aware local feature detector. In *Proceedings of the IEEE/CVF Winter Conference on Applications of Computer Vision*, pages 3362–3372, 2024. 3
- [76] Zhenjun Zhao and Ben M Chen. Benchmark for evaluating initialization of visual-inertial odometry. In *2023 42nd Chinese Control Conference (CCC)*, pages 3935–3940. IEEE, 2023.
- [77] Zhenjun Zhao, Heng Yang, Bangyan Liao, Yingping Zeng, Shaocheng Yan, Yingdong Gu, Peidong Liu, Yi Zhou, Haoang Li, and Javier Civera. Advances in global solvers for 3d vision. *arXiv preprint arXiv:2602.14662*, 2026. 3
- [78] Pan Zhou, Xingyu Xie, Zhouchen Lin, and Shuicheng Yan. Towards understanding convergence and generalization of adamw. *IEEE transactions on pattern analysis and machine intelligence*, 46(9):6486–6493, 2024. 3

DP-FedAdamW: An Efficient Optimizer for Differentially Private Federated Large Models

Supplementary Material

9. More Implementation Detail

9.1. More Results

Swin-Tiny/Base on CIFAR-10. Table 10 reports the averaged test accuracy on CIFAR-10 for six different DPFL methods evaluated on Swin-Tiny and Swin-Base, under two data heterogeneity levels (Dirichlet $\alpha=0.6$ and $\alpha=0.1$). Overall, DP-FedAdamW consistently achieves the best performance, while Swin-Base is markedly more accurate than Swin-Tiny and all methods degrade when the data becomes more heterogeneous (smaller α). For Swin-Base with $\alpha=0.1$, DP-FedAdamW attains 90.68% test accuracy, outperforming DP-FedSAM (89.82%) and DP-FedAvg (88.23%), even though DP-FedSAM needs roughly twice the privacy budget.

Table 10. Averaged test accuracy (%) comparison on CIFAR-10. Assuming DP-FedAvg is (ϵ, δ) -DP, all other methods share this budget except DP-FedSAM, which is approximately $(2\epsilon, \delta)$ -DP.

Method	Swin-Tiny		Swin-Base		Privacy Budget
	$\alpha=0.6$	$\alpha=0.1$	$\alpha=0.6$	$\alpha=0.1$	
DP-FedAvg	82.93 \pm 0.53	78.24 \pm 0.59	89.56 \pm 0.47	88.23 \pm 0.44	(ϵ, δ)
DP-SCAFFOLD	82.85 \pm 0.50	78.53 \pm 0.54	90.07 \pm 0.48	89.08 \pm 0.62	(ϵ, δ)
DP-FedAvg-LS	83.94 \pm 0.62	79.67 \pm 0.68	90.97 \pm 0.52	90.14 \pm 0.56	(ϵ, δ)
DP-FedSAM	84.05 \pm 0.51	80.36 \pm 0.57	91.25 \pm 0.54	89.82 \pm 0.60	$(2\epsilon, \delta)$
DP-LocalAdamW	83.73 \pm 0.58	79.28 \pm 0.64	90.84 \pm 0.39	89.08 \pm 0.41	(ϵ, δ)
DP-FedAdamW	84.23\pm0.32	81.23\pm0.39	91.79\pm0.34	90.68\pm0.38	(ϵ, δ)

Noise multiplier results. To further analyze the impact of privacy noise on algorithm performance, we evaluate different noise multipliers $\sigma \in \{0.5, 1.0, 1.5, 2.0\}$ on CIFAR-100 using the Swin-Base model under Dirichlet $\alpha=0.6$ and $\alpha=0.1$. As shown in Table 11, increasing the noise multiplier consistently degrades test accuracy for all methods, while DP-FedAdamW maintains the best performance across all σ . Although $\sigma=0.5$ yields the highest accuracy, it also consumes a much larger privacy budget. In contrast, setting $\sigma=1$ significantly strengthens the formal privacy guarantee while only causing a small drop in accuracy, whereas larger noise levels ($\sigma \geq 1.5$) lead to a much more pronounced loss in utility. Therefore, we adopt $\sigma=1$ as the default noise multiplier in our main experiments, as it offers a favorable privacy–utility trade-off.

Table 11. Test accuracy (%) on CIFAR-100 with Swin-Base under different noise multipliers σ .

Method	$\alpha = 0.6$				$\alpha = 0.1$			
	$\sigma=0.5$	$\sigma=1$	$\sigma=1.5$	$\sigma=2$	$\sigma=0.5$	$\sigma=1$	$\sigma=1.5$	$\sigma=2$
DP-FedAvg	67.23 \pm 0.33	65.61 \pm 0.27	63.78 \pm 0.34	60.22 \pm 0.64	62.49 \pm 0.26	60.77 \pm 0.32	57.85 \pm 0.48	54.34 \pm 0.79
DP-SCAFFOLD	70.41 \pm 0.25	68.03 \pm 0.55	64.64 \pm 0.48	63.14 \pm 0.58	66.72 \pm 0.38	65.34 \pm 0.49	61.73 \pm 0.44	58.23 \pm 0.66
DP-FedAvg-LS	70.93 \pm 0.40	68.80 \pm 0.52	66.52 \pm 0.43	64.77 \pm 0.63	68.36 \pm 0.39	66.08 \pm 0.56	62.87 \pm 0.52	59.98 \pm 0.58
DP-FedSAM	72.55 \pm 0.22	70.44 \pm 0.57	67.45 \pm 0.33	65.75 \pm 0.69	67.94 \pm 0.51	66.28 \pm 0.64	62.21 \pm 0.60	60.84 \pm 0.71
DP-LocalAdamW	70.74 \pm 0.13	68.33 \pm 0.33	66.46 \pm 0.53	64.10 \pm 0.60	67.35 \pm 0.31	65.28 \pm 0.39	60.55 \pm 0.43	58.78 \pm 0.74
DP-FedAdamW	73.62\pm0.36	71.58\pm0.30	68.52\pm0.45	66.79\pm0.51	69.22\pm0.37	67.45\pm0.26	63.28\pm0.42	61.05\pm0.61

9.2. Datasets

Vision datasets. We evaluate our methods on three widely used image classification benchmarks: CIFAR-10, CIFAR-100, and Tiny-ImageNet in Table 12. CIFAR-10 and CIFAR-100 [28] each contain 60,000 natural images of size 32×32 , split into 50,000 training and 10,000 test examples. CIFAR-10 comprises 10 coarse-grained object categories, whereas CIFAR-100 has finer labeling with 100 fine-grained categories organized into 20 superclasses. Tiny-ImageNet [30] is a downsampled subset of ImageNet with 200 classes, where each class contains 500 training images and 50 validation images of size 64×64 .

Language datasets. For natural language understanding, we experiment on four tasks from the GLUE [67] benchmark: SST-2, QQP, QNLI, and MNLI (Table 13). SST-2 is a binary sentiment classification task over movie reviews. QQP is a paraphrase identification task that determines whether two Quora questions express the same semantic intent. QNLI is a

Table 12. Summary of the vision datasets used in our experiments.

Dataset	#Classes	Image Size	Train / Test
CIFAR-10 [28]	10	32×32	50,000 / 10,000
CIFAR-100 [28]	100	32×32	50,000 / 10,000
Tiny-ImageNet [30]	200	64×64	100,000 / 10,000

binary classification task that predicts whether a candidate sentence contains the answer to a given question. MNLI is a three-way natural language inference benchmark (entailment, contradiction, neutral) covering multiple genres of text. We follow the standard GLUE data splits and evaluation protocols.

Table 13. Summary of GLUE datasets used in our experiments.

Dataset	Task Type	#Classes	Train/Test
SST-2	Sentiment Classification (binary)	2	67,349 / 1,821
QQP	Duplicate Question Detection (binary)	2	363,846 / 390,965
QNLI	Question-Answer NLI (binary)	2	104,743 / 5,463
MNLI	Natural Language Inference (entailment)	3	392,702 / 9,815

9.3. Models

We study three representative architecture families, covering five specific models in total, as summarized in Table 14.

(1) **ResNet-18**. We adopt a ResNet-18 with Group Normalization (GN), where all Batch Normalization layers are replaced by GN to avoid dependence on batch statistics, which is more suitable for federated and differentially private training. To adapt CIFAR-10/100, we follow standard practices and modify the stem by replacing the original 7×7 convolution with a 3×3 kernel and removing the initial downsampling layers (i.e., the stride-2 convolution and max-pooling layer).

(2) **ViT-Base**. We use the standard Vision Transformer Base (ViT-Base) architecture, which splits an input image into non-overlapping 16×16 patches and linearly embeds them into a sequence of tokens with a prepended class token. The token sequence is processed by 12 Transformer encoder layers with multi-head self-attention and MLP blocks, and the final class token representation is fed to a linear classifier to produce the output logits.

(3) **Swin-Tiny**. Swin-Tiny is a hierarchical Vision Transformer that uses shifted window self-attention. The model consists of four stages with depths [2, 2, 6, 2], embedding dimensions [96, 192, 384, 768], and attention heads [3, 6, 12, 24]. Images are partitioned into 4×4 patches, and each stage applies window-based attention with window size 7 and an MLP ratio of 4, using LayerNorm and relative positional bias. DropPath regularization with depth-scaled rates is used, and the final features are aggregated by global pooling and passed to a linear classifier.

(4) **Swin-Base**. Swin-Base is a larger variant of Swin-Tiny, sharing the same hierarchical shifted-window design. It is configured with four stages of depths [2, 2, 18, 2], embedding dimensions [128, 256, 512, 1024], and attention heads [4, 8, 16, 32], using a patch size of 4×4 , window size 7, and MLP ratio 4. Similar to Swin-Tiny, the final stage features are pooled globally and fed into a linear classifier to generate predictions.

(5) **RoBERTa-Base**. We use the RoBERTa-Base architecture, which follows the standard Transformer encoder design with 12 layers, 12 attention heads, and a hidden size of 768. It employs byte-pair encoding (BPE) tokenization and is pre-trained with a masked language modeling objective on large-scale corpora using dynamic masking. The final representation corresponding to the classification token is fed into a task-specific linear classifier.

Table 14. Overview of the model architectures used in our experiments. “Depth” denotes the total number of layers (blocks for ResNet/Swin, encoder layers for ViT/RoBERTa), and “Stages” denotes the number of blocks per stage for hierarchical models.

Model	Family	Depth	Stages	Width / Dim	Heads
ResNet-18 (GN)	CNN	18	[2, 2, 2, 2]	[64, 128, 256, 512]	–
ViT-Base	ViT Transformer	12	–	768 hidden, 3072 MLP	12 / layer
Swin-Tiny	Swin Transformer	12	[2, 2, 6, 2]	[96, 192, 384, 768]	[3, 6, 12, 24]
Swin-Base	Swin Transformer	24	[2, 2, 18, 2]	[128, 256, 512, 1024]	[4, 8, 16, 32]
RoBERTa-Base	NLP Transformer	12	–	768 hidden, 3072 FFN	12 / layer

Algorithm 2 DP-LocalAdamW

```

1: Initial initial model  $\theta^0$ ; rounds  $T$ ; local steps  $K$ ; step size  $\eta$ ; weight decay  $\lambda$ ; AdamW  $(\beta_1, \beta_2, \epsilon)$ ; clip norm  $C$ ; noise multiplier  $\sigma$ ;  $S$  clients per round
2: for  $t = 1$  to  $T$  do
3:   for selected clients  $i = 1, \dots, S$  in parallel do
4:      $\theta_i^{t,0} \leftarrow \theta^t$ ;  $\mathbf{m}_i^{t,0} \leftarrow \mathbf{0}$ ;  $\mathbf{v}_i^{t,0} \leftarrow \mathbf{0}$ 
5:     for  $k = 1$  to  $K$  do
6:       sample  $\mathcal{D}_i^k \subset \mathcal{D}_i$  of size  $\lfloor sR \rfloor$ 
7:       for each sample  $j \in \mathcal{D}_i^k$  do
8:          $g_{ij} \leftarrow \nabla f_i(\theta_i^{t,k}; \xi_{ij})$ 
9:          $\bar{g}_{ij} \leftarrow g_{ij} / \max(1, \|g_{ij}\|_2 / C)$ 
10:      end for
11:       $\tilde{g}_i^{t,k} \leftarrow \frac{1}{sR} \sum_{j \in \mathcal{D}_i^k} \bar{g}_{ij} + \frac{C}{sR} \mathcal{N}(0, \sigma^2 C^2 I)$ 
12:       $\mathbf{m}_i^{t,k} \leftarrow \beta_1 \mathbf{m}_i^{t,k-1} + (1 - \beta_1) \tilde{g}_i^{t,k}$ 
13:       $\mathbf{v}_i^{t,k} \leftarrow \beta_2 \mathbf{v}_i^{t,k-1} + (1 - \beta_2) \tilde{g}_i^{t,k} \odot \tilde{g}_i^{t,k}$ 
14:       $\hat{\mathbf{m}}_i^{t,k} \leftarrow \mathbf{m}_i^{t,k} / (1 - \beta_1^k)$ 
15:       $\hat{\mathbf{v}}_i^{t,k} \leftarrow \mathbf{v}_i^{t,k} / (1 - \beta_2^k)$ 
16:       $\theta_i^{t,k+1} \leftarrow \theta_i^{t,k} - \eta (\hat{\mathbf{m}}_i^{t,k} / (\sqrt{\hat{\mathbf{v}}_i^{t,k}} + \epsilon) - \lambda \theta_i^{t,k})$ 
17:    end for
18:    Clients send  $(\theta_i^{t,K} - \theta_i^{t,0})$  to server
19:  end for
20:   $\theta^{t+1} \leftarrow \theta^t + \frac{1}{S} \sum_{i=1}^S (\theta_i^{t,K} - \theta_i^{t,0})$ 
21:  Broadcast  $\theta^{t+1}$  to clients
22: end for

```

Table 15. Federated configurations for vision models across CIFAR-10/100 and Tiny-ImageNet. We report the number of clients N , communication rounds T , local steps K , client participation rate l , local batch size sR , DP noise multiplier σ , failure probability δ , and LoRA hyperparameters (r, α_L) and dropout rate.

Dataset	Model	N	T	K	l	sR	σ	δ	r (LoRA)	α_L (LoRA)	Dropout
CIFAR-10	ResNet-18 (GN)	50	300	50	0.2	50	1.0	10^{-5}	16	32	0.1
	ViT-Base	50	100	20	0.1	16	1.0	10^{-5}	16	32	0.1
	Swin-Tiny/Base	50	100	20	0.1	16	1.0	10^{-5}	16	32	0.1
CIFAR-100	ResNet-18 (GN)	50	300	50	0.2	50	1.0	10^{-5}	16	32	0.1
	ViT-Base	50	100	20	0.1	16	1.0	10^{-5}	16	32	0.1
	Swin-Tiny/Base	50	100	20	0.1	16	1.0	10^{-5}	16	32	0.1
Tiny-ImageNet	Swin-Tiny/Base	50	100	20	0.1	16	1.0	10^{-6}	16	32	0.1

9.4. Complete Configuration

Federated setup. In all experiments, we fine-tune the models using parameter-efficient Low-Rank Adaptation (LoRA). We then detail the federated learning configurations adopted in our experiments. Table 15 specifies the settings for all vision benchmarks, including the number of clients N , communication rounds T , local update steps K , client participation rate l , local batch size sR , DP noise multiplier σ , failure probability δ , and LoRA hyperparameters (r, α_L) . Table 17 reports the corresponding configuration for the GLUE benchmarks with RoBERTa-Base and LoRA, using the same federated parameters while additionally documenting the maximum sequence length and dropout rate.

Other setup. DP-FedAvg, DP-SCAFFOLD, DP-FedAvg-LS, and DP-FedSAM adopt learning rates selected from $\{10^{-2}, 3 \times 10^{-2}, 5 \times 10^{-2}, 10^{-1}, 3 \times 10^{-1}\}$ with a fixed weight decay of 0.001. For DP-FedSAM, the SAM perturbation ρ is selected via grid search over $\{0.01, 0.05, 0.1, 0.5\}$. For DP-LocalAdamW and DP-FedAdamW, the learning rate is chosen from $\{10^{-4}, 2 \times 10^{-4}, 3 \times 10^{-4}, 5 \times 10^{-4}, 8 \times 10^{-4}, 10^{-3}\}$, combined with weight decay in $\{0.01, 0.001\}$ and standard AdamW parameters $(\beta_1=0.9, \beta_2=0.999)$. We employ cosine learning-rate decay throughout, and DP-FedAdamW

Table 16. Federated configurations for RoBERTa-Base with LoRA on GLUE tasks. We report the number of clients N , communication rounds T , local steps K , client participation rate l , local batch size sR , DP noise multiplier σ , failure probability δ , and LoRA hyperparameters (r, α_L) , as well as the maximum sequence length and dropout rate.

Dataset	Model	N	T	K	l	sR	σ	δ	r (LoRA)	α_L (LoRA)	Length_max	Dropout
SST-2	RoBERTa-Base	4	100	20	1.0	16	1.0	10^{-5}	16	32	128	0.1
QQP		4	100	20	1.0	16	1.0	10^{-6}	16	32	128	0.1
QNLI		4	100	20	1.0	16	1.0	10^{-5}	16	32	128	0.1
MNLI		4	100	20	1.0	16	1.0	10^{-6}	16	32	128	0.1

additionally uses parameter $\gamma=0.5$ and weight decay $\lambda=0.01$. For all visual fine-tuning tasks, we initialize from official ImageNet-22K pre-trained weights to ensure consistency across methods. Across all tasks, the gradient clipping threshold is chosen by grid search over $\{0.05, 0.1, 0.2, 0.3, 0.5\}$, and we find that larger clipping values can trigger gradient explosion. To obtain a simple and robust configuration across all benchmarks, we therefore adopt a unified clipping threshold of $C=0.1$.

Table 17. Hyperparameter configuration of ResNet-18 (CIFAR-10/100) across different algorithms.

Method	Local Optimizer	η	β_1	β_2	Weight Decay
DP-FedAvg	SGD	10^{-1}	-	-	0.001
DP-SCAFFOLD	SGD	10^{-1}	-	-	0.001
DP-FedAvg-LS	SGD	10^{-1}	-	-	0.001
DP-FedSAM	SAM	10^{-1}	-	-	0.001
DP-LocalAdamW	AdamW	3×10^{-4}	0.9	0.999	0.01
DP-FedAdamW	AdamW	3×10^{-4}	0.9	0.999	0.01

10. DP-LocalAdamW Algorithm

For completeness, we provide in Algorithm 2 the full local training procedure of **DP-LocalAdamW**.

11. Theoretical Analysis Details

11.1. Proof of Theorem 1 and Convergence Analysis

Assumption A.1 (Smoothness). (Smoothness) The non-convex f_i is a L -smooth function for all $i \in [m]$, i.e., $\|\nabla f_i(\theta_1) - \nabla f_i(\theta_2)\| \leq L\|\theta_1 - \theta_2\|$, for all $\theta_1, \theta_2 \in \mathbb{R}^d$.

Assumption A.2 (Bounded Stochastic Gradient). $\mathbf{g}_i^t = \nabla f_i(\theta_i^t, \xi_i^t)$ computed by using a sampled mini-batch data ξ_i^t in the local client i is an unbiased estimator of ∇f_i with bounded variance, i.e., $\mathbb{E}_{\xi_i^t}[\mathbf{g}_i^t] = \nabla f_i(\theta_i^t)$ and $\mathbb{E}_{\xi_i^t} \|\mathbf{g}_i^t - \nabla f_i(\theta_i^t)\|^2 \leq \sigma_i^2$, for all $\theta_i^t \in \mathbb{R}^d$.

Assumption A.3 (Bounded Stochastic Gradient II). Each element of stochastic gradient \mathbf{g}_i^t is bounded, i.e., $\|\mathbf{g}_i^t\|_\infty = \|f_i(\theta_i^t, \xi_i^t)\|_\infty \leq G_g$, for all $\theta_i^t \in \mathbb{R}^d$ and any sampled mini-batch data ξ_i^t .

Assumption A.4 (Bounded Heterogeneity). The gradient dissimilarity between clients is bounded: $\|\nabla f_i(\theta_1) - \nabla f_i(\theta_2)\|^2 \leq \sigma_g^2$, for all $\theta \in \mathbb{R}^d$.

In this section, we give the theoretical analysis of our proposed DP-FedAdamW algorithm. Firstly we state some standard assumptions for the non-convex function F .

We use the common gradient bound condition in our proof. Then we can upper bound G_ϑ as:

$$\begin{aligned}
 G_\vartheta &= \left\{ \|\vartheta_i^{t,k}\|_\infty \right\} = \left\{ \left\| \frac{1}{\sqrt{(1 - \beta_1^k)^2 / (1 - \beta_2^t) \mathbf{v}_i^{t,k} + \epsilon}} \right\|_\infty \right\} \\
 &= \left\{ \left\| \frac{1}{\sqrt{(1 - \beta_1^k)^2 / (1 - \beta_2^t) (\beta_2 \mathbf{v}_i^{t,k-1} + (1 - \beta_2) \mathbf{g}_i^{t,k} \cdot \mathbf{g}_i^{t,k}) + \epsilon}} \right\|_\infty \right\}.
 \end{aligned}$$

$\sqrt{(1 - \beta_1^k)^2 / (1 - \beta_2^t)(\beta_2 \mathbf{v}_i^{t,k-1} + (1 - \beta_2) \mathbf{g}_i^{t,k} \cdot \mathbf{g}_i^{t,k})}$ is bounded as:

$$\left\| \sqrt{(1 - \beta_1^k)^2 / (1 - \beta_2^t)(\beta_2 \mathbf{v}_i^{t,k-1} + (1 - \beta_2) \mathbf{g}_i^{t,k} \cdot \mathbf{g}_i^{t,k})} \right\|_\infty \leq G_g. \quad (15)$$

Thus we bound G_ϑ as $\frac{1}{G_g} \leq G_\vartheta \leq \frac{1}{\epsilon}$.

11.2. Main Lemmas

Lemma 1. Suppose $\{X_1, \dots, X_\tau\} \subset \mathbb{R}^d$ be random variables that are potentially dependent. If their marginal means and variances satisfy $\mathbb{E}[X_i] = \mu_i$ and $\mathbb{E}[\|X_i - \mu_i\|^2] \leq \sigma^2$, then it holds that

$$\mathbb{E} \left[\left\| \sum_{i=1}^{\tau} X_i \right\|^2 \right] \leq \left\| \sum_{i=1}^{\tau} \mu_i \right\|^2 + \tau^2 \sigma^2.$$

If they are correlated in the Markov way such that $\mathbb{E}[X_i | X_{i-1}, \dots, X_1] = \mu_i$ and $\mathbb{E}[\|X_i - \mu_i\|^2 | \mu_i] \leq \sigma^2$, i.e., the variables $\{X_i - \mu_i\}$ form a martingale. Then the following tighter bound holds:

$$\mathbb{E} \left[\left\| \sum_{i=1}^{\tau} X_i \right\|^2 \right] \leq 2\mathbb{E} \left[\left\| \sum_{i=1}^{\tau} \mu_i \right\|^2 \right] + 2\tau\sigma^2.$$

Lemma 2. Given vectors $v_1, \dots, v_N \in \mathbb{R}^d$ and $\bar{v} = \frac{1}{N} \sum_{i=1}^N v_i$, if we sample $\mathcal{S} \subset \{1, \dots, N\}$ uniformly randomly such that $|\mathcal{S}| = S$, then it holds that

$$\mathbb{E} \left[\left\| \frac{1}{S} \sum_{i \in \mathcal{S}} v_i \right\|^2 \right] = \|\bar{v}\|^2 + \frac{N-S}{S(N-1)} \frac{1}{N} \sum_{i=1}^N \|v_i - \bar{v}\|^2.$$

Proof. Letting $\mathbb{I}\{i \in \mathcal{S}\}$ be the indicator for the event $i \in \mathcal{S}$, we prove this lemma by direct calculation as follows:

$$\begin{aligned} \mathbb{E} \left[\left\| \frac{1}{S} \sum_{i \in \mathcal{S}} v_i \right\|^2 \right] &= \mathbb{E} \left[\left\| \frac{1}{S} \sum_{i=1}^N v_i \mathbb{I}\{i \in \mathcal{S}\} \right\|^2 \right] \\ &= \frac{1}{S^2} \mathbb{E} \left[\left(\sum_i \|v_i\|^2 \mathbb{I}\{i \in \mathcal{S}\} + 2 \sum_{i < j} v_i^\top v_j \mathbb{I}\{i, j \in \mathcal{S}\} \right) \right] \\ &= \frac{1}{SN} \sum_{i=1}^N \|v_i\|^2 + \frac{1}{S^2} \frac{S(S-1)}{N(N-1)} 2 \sum_{i < j} v_i^\top v_j \\ &= \frac{1}{SN} \sum_{i=1}^N \|v_i\|^2 + \frac{1}{S^2} \frac{S(S-1)}{N(N-1)} \left(\left\| \sum_{i=1}^N v_i \right\|^2 - \sum_{i=1}^N \|v_i\|^2 \right) \\ &= \frac{N-S}{S(N-1)} \frac{1}{N} \sum_{i=1}^N \|v_i\|^2 + \frac{N(S-1)}{S(N-1)} \|\bar{v}\|^2 \\ &= \frac{N-S}{S(N-1)} \frac{1}{N} \sum_{i=1}^N \|v_i - \bar{v}\|^2 + \|\bar{v}\|^2. \end{aligned}$$

□

11.3. Basic Assumptions and Notations

Let $\mathcal{F}^0 = \emptyset$ and $\mathcal{F}_i^{t,k} := \sigma\left(\left\{\boldsymbol{\theta}_i^{t,j}\right\}_{0 \leq j \leq k} \cup \mathcal{F}^t\right)$ and $\mathcal{F}^{t+1} := \sigma\left(\cup_i \mathcal{F}_i^{t,K}\right)$ for all $t \geq 0$ where $\sigma(\cdot)$ indicates the σ -algebra. Let $\mathbb{E}_t[\cdot] := \overline{\mathbb{E}}[\cdot | \mathcal{F}^t]$ be the expectation, conditioned on the filtration \mathcal{F}^t , with respect to the random variables $\left\{\mathcal{S}^t, \left\{\xi_i^{t,k}\right\}_{1 \leq i \leq N, 0 \leq k < K}\right\}$ in the t -th iteration. We also use $\mathbb{E}[\cdot]$ to denote the global expectation over all randomness in algorithms. Through out the proofs, we use \sum_i to represent the sum over $i \in \{1, \dots, N\}$, while $\sum_{i \in \mathcal{S}^t}$ denotes the sum over $i \in \mathcal{S}^t$. Similarly, we use \sum_k to represent the sum of $k \in \{0, \dots, K-1\}$. For all $t \geq 0$, we define the following auxiliary variables to facilitate proofs:

$$\begin{aligned}\mathcal{E}_t &:= \mathbb{E} \left[\left\| \nabla f(\boldsymbol{\theta}^t) \odot \frac{1}{SK} \sum_{i \in \mathcal{S}^t} \sum_{k=1}^K \vartheta_i^{t,k} - \Delta_G^{t+1} \right\|^2 \right], \\ U_t &:= \frac{1}{NK} \sum_i \sum_k \mathbb{E} \left[\left\| \boldsymbol{\theta}_i^{t,k} - \boldsymbol{\theta}^t \right\|^2 \right], \\ \xi_i^{t,k} &:= \mathbb{E} \left[\boldsymbol{\theta}_i^{t,k+1} - \boldsymbol{\theta}_i^{t,k} \mid \mathcal{F}_i^{t,k} \right], \\ \Xi_t &:= \frac{1}{N} \sum_{i=1}^N \mathbb{E} \left[\left\| \xi_i^{t,0} \right\|^2 \right].\end{aligned}$$

Throughout the Appendix, we let $\Delta := f(\boldsymbol{\theta}^0) - f^*, G_0 := \frac{1}{N} \sum_i \|\nabla f_i(\boldsymbol{\theta}^0)\|^2$, $\boldsymbol{\theta}^{-1} := \boldsymbol{\theta}^0$ and $\mathcal{E}_{-1} := \mathbb{E} \left[\left\| \nabla f(\boldsymbol{\theta}^0) - g^0 \right\|^2 \right]$. We will use the following foundational lemma for all our algorithms.

11.4. Proof of Theorem 1

Lemma 3. *Under Assumption A.1, if $\gamma L \leq \frac{1}{24}$, the following holds all $t \geq 0$:*

$$\mathbb{E} [f(\boldsymbol{\theta}^{t+1})] \leq \mathbb{E} [f(\boldsymbol{\theta}^t)] - \frac{11\gamma}{24} \mathbb{E} \left[\left\| \nabla f(\boldsymbol{\theta}^t) \right\|^2 \right] + \frac{13\gamma}{24} \mathcal{E}_t + \frac{13\gamma}{24} \frac{\sigma^2 G_g^2}{s^2 R^2}.$$

Proof. Since f is L -smooth, we have

$$\begin{aligned}f(\boldsymbol{\theta}^{t+1}) &\leq f(\boldsymbol{\theta}^t) + \langle \nabla f(\boldsymbol{\theta}^t), \boldsymbol{\theta}^{t+1} - \boldsymbol{\theta}^t \rangle + \frac{L}{2} \left\| \boldsymbol{\theta}^{t+1} - \boldsymbol{\theta}^t \right\|^2 \\ &\leq f(\boldsymbol{\theta}^t) + \gamma \langle \nabla f(\boldsymbol{\theta}^t), \Delta_G^{t+1} \rangle + \frac{L\gamma^2}{2} \left\| \Delta_G^{t+1} \right\|^2 \\ &= f(\boldsymbol{\theta}^t) - \gamma \left\| \nabla f(\boldsymbol{\theta}^t) \odot \frac{1}{SK} \sum_{i \in \mathcal{S}^t} \sum_{k=1}^K \vartheta_i^{t,k} \right\|^2 + \gamma \left\langle \nabla f(\boldsymbol{\theta}^t), \nabla f(\boldsymbol{\theta}^t) \odot \frac{1}{SK} \sum_{i \in \mathcal{S}^t} \sum_{k=1}^K \vartheta_i^{t,k} - \Delta_G^{t+1} \right\rangle \\ &\quad + \frac{L\gamma^2}{2} \left\| \Delta_G^{t+1} \right\|^2.\end{aligned}$$

Since $\boldsymbol{\theta}^{t+1} = \boldsymbol{\theta}^t - \gamma \Delta_G^{t+1}$, using Young's inequality, we further have

$$\begin{aligned}
& \mathbb{E}f(\boldsymbol{\theta}^{t+1}) \\
& \leq f(\boldsymbol{\theta}^t) - (\gamma G_g^2 - \frac{\gamma}{2}) \|\nabla f(\boldsymbol{\theta}^t)\|^2 + \frac{\gamma}{2} \left\| \nabla f(\boldsymbol{\theta}^t) \odot \frac{1}{SK} \sum_{i \in S^t} \sum_{k=1}^K \vartheta_i^{t,k} - \Delta_G^{t+1} \right\|^2 \\
& + L\gamma^2 \left(\left\| \nabla f(\boldsymbol{\theta}^t) \odot \frac{1}{SK} \sum_{i \in S^t} \sum_{k=1}^K \vartheta_i^{t,k} \right\|^2 + \left\| \nabla f(\boldsymbol{\theta}^t) \odot \frac{1}{SK} \sum_{i \in S^t} \sum_{k=1}^K \vartheta_i^{t,k} - \Delta_G^{t+1} \right\|^2 \right) \\
& \leq f(\boldsymbol{\theta}^t) - (\gamma G_g^2 - \frac{\gamma}{2} - L\gamma^2 G_g^2) \|\nabla f(\boldsymbol{\theta}^t)\|^2 + \frac{13\gamma}{24} \left\| \nabla f(\boldsymbol{\theta}^t) \odot \frac{1}{SK} \sum_{i \in S^t} \sum_{k=1}^K \vartheta_i^{t,k} - \Delta_G^{t+1} \right\|^2 + \frac{13\gamma}{24} \frac{\sigma^2 G_g^2}{s^2 R^2} \\
& \leq f(\boldsymbol{\theta}^t) - \frac{11\gamma}{24} \|\nabla f(\boldsymbol{\theta}^t)\|^2 + \frac{13\gamma}{24} \left\| \nabla f(\boldsymbol{\theta}^t) \odot \frac{1}{SK} \sum_{i \in S^t} \sum_{k=1}^K \vartheta_i^{t,k} - \Delta_G^{t+1} \right\|^2 + \frac{13\gamma}{24} \frac{\sigma^2 G_g^2}{s^2 R^2},
\end{aligned}$$

where the last inequality is due to $\gamma L \leq \frac{1}{24}$, $-(\gamma G_g^2 - \frac{\gamma}{2} - L\gamma^2 G_g^2) \leq -\frac{11\gamma}{24}$. Taking the global expectation, we finish the proof. \square

Lemma 4. If $\gamma L \leq \frac{\gamma}{6}$, the following holds for $t \geq 1$:

$$\mathcal{E}_t \leq \left(1 - \frac{8\gamma}{9}\right) \mathcal{E}_{t-1} + \frac{4\gamma^2 L^2}{\gamma} \mathbb{E} \left[\|\nabla f(\boldsymbol{\theta}^{t-1})\|^2 \right] + \frac{2\gamma^2 \sigma_l^2}{SK \epsilon^2} + 4\frac{\gamma}{\epsilon^2} L^2 U_t.$$

Additionally, it holds for $t = 0$ that

$$\mathcal{E}_0 \leq (1 - \gamma) \mathcal{E}_{-1} + \frac{2\gamma^2 \sigma_l^2}{SK} + 4\gamma L^2 U_0.$$

Proof. For $t > 1$,

$$\begin{aligned}
\mathcal{E}_t &= \mathbb{E} \left[\left\| \frac{1}{SK} \sum_{i \in S^t} \sum_{k=1}^K \nabla f(\boldsymbol{\theta}^t) \odot \vartheta_i^{t,k} - \Delta_G^{t+1} \right\|^2 \right] \\
&= \mathbb{E} \left[\left\| (1 - \gamma) \left(\frac{1}{SK} \sum_{i \in S^t} \sum_{k=1}^K \nabla f(\boldsymbol{\theta}^t) \odot \vartheta_i^{t,k} - \Delta_G^t \right) + \gamma \left(\frac{1}{SK} \sum_{i \in S^t} \sum_{k=1}^K \nabla f(\boldsymbol{\theta}^t) \odot \vartheta_i^{t,k} - \frac{1}{SK} \sum_{i \in S^t} \sum_{k=1}^K g_i^{t,k} \odot \vartheta_i^{t,k} \right) \right\|^2 \right] \\
&\leq \mathbb{E} \left[\left\| (1 - \gamma) \left(\frac{1}{SK} \sum_{i \in S^t} \sum_{k=1}^K \nabla f(\boldsymbol{\theta}^t) \odot \vartheta_i^{t,k} - \Delta_G^t \right) \right\|^2 \right] + \gamma^2 \frac{1}{\epsilon^2} \mathbb{E} \left[\left\| \nabla f(\boldsymbol{\theta}^t) - \frac{1}{SK} \sum_{i \in S^t} \sum_{k=1}^K g_i^{t,k} \right\|^2 \right] \\
&+ 2\gamma \mathbb{E} \left[\left\langle (1 - \gamma) \left(\frac{1}{SK} \sum_{i \in S^t} \sum_{k=1}^K \nabla f(\boldsymbol{\theta}^t) \odot \vartheta_i^{t,k} - \Delta_G^t \right), \frac{1}{SK} \sum_{i \in S^t} \sum_{k=1}^K \nabla f(\boldsymbol{\theta}^t) \odot \vartheta_i^{t,k} - \frac{1}{SK} \sum_{i \in S^t} \sum_{k=1}^K g_i^{t,k} \odot \vartheta_i^{t,k} \right\rangle \right].
\end{aligned}$$

Note that $\left\{ \nabla F(\boldsymbol{\theta}_i^{t,k}; \boldsymbol{c}_i^{t,k}) \right\}_{0 \leq k < K}$ are sequentially correlated. Applying the AM-GM inequality and Lemma 1, we have

$$\mathcal{E}_t \leq \left(1 + \frac{\gamma}{2}\right) \mathbb{E} \left[\|(1 - \gamma) (\nabla f(\boldsymbol{\theta}^t) - \Delta_G^t)\|^2 \right] + 2\frac{\gamma}{\epsilon^2} L^2 U_t + 2\frac{\gamma^2}{\epsilon^2} \left(\frac{\sigma_l^2}{SK} + L^2 U_t \right).$$

Using the AM-GM inequality again and Assumption A.1, we have

$$\begin{aligned}
\mathcal{E}_t &\leq (1 - \gamma)^2 \left(1 + \frac{\gamma}{2}\right) \left[\left(1 + \frac{\gamma}{2}\right) \mathcal{E}_{t-1} + \left(1 + \frac{2}{\gamma}\right) L^2 \mathbb{E} \left[\|\boldsymbol{\theta}^t - \boldsymbol{\theta}^{t-1}\|^2 \right] \right] + \frac{2\gamma^2 \sigma_l^2}{SK \epsilon^2} + 4\frac{\gamma}{\epsilon^2} L^2 U_t \\
&\leq (1 - \gamma) \mathcal{E}_{t-1} + \frac{2}{\gamma} L^2 \mathbb{E} \left[\|\boldsymbol{\theta}^t - \boldsymbol{\theta}^{t-1}\|^2 \right] + \frac{2\gamma^2 \sigma_l^2}{\epsilon^2 SK} + 4\frac{\gamma}{\epsilon^2} L^2 U_t \\
&\leq \left(1 - \frac{8\gamma}{9}\right) \mathcal{E}_{t-1} + 4\frac{\gamma^2 L^2}{\gamma} \mathbb{E} \left[\|\nabla f(\boldsymbol{\theta}^{t-1})\|^2 \right] + \frac{2\gamma^2 \sigma_l^2}{\epsilon^2 SK} + 4\frac{\gamma}{\epsilon^2} L^2 U_t,
\end{aligned}$$

where we plug in $\|\boldsymbol{\theta}^t - \boldsymbol{\theta}^{t-1}\|^2 \leq 2\gamma^2 \left(\|\nabla f(\boldsymbol{\theta}^{t-1})\|^2 + \|\Delta_G^t - \nabla f(\boldsymbol{\theta}^{t-1})\|^2 \right)$ and use $\gamma L \leq \frac{\gamma}{6}$ in the last inequality. Similarly for $t = 0$,

$$\begin{aligned} \mathcal{E}_0 &\leq \left(1 + \frac{\gamma}{2}\right) \mathbb{E} \left[\|(1 - \gamma)(\nabla f(\boldsymbol{\theta}^0) - g^0)\|^2 \right] + 2\frac{\gamma}{\epsilon^2} L^2 U_0 + 2\frac{\gamma^2}{\epsilon^2} \left(\frac{\sigma_l^2}{SK} + L^2 U_0 \right) \\ &\leq (1 - \gamma)\mathcal{E}_{-1} + \frac{2\gamma^2 \sigma_l^2}{SK\epsilon^2} + 4\frac{\gamma}{\epsilon^2} L^2 U_0. \end{aligned}$$

□

Lemma 5. *If $\eta L K \leq \frac{1}{\gamma}$, the following holds for $t \geq 0$:*

$$U_t \leq 2eK^2 \Xi_t + K\eta^2 \gamma^2 \frac{1}{\epsilon^2} \sigma_l^2 (1 + 2K^3 L^2 \eta^2 \gamma^2).$$

Proof. Recall that $\xi_i^{t,k} := \mathbb{E} \left[\boldsymbol{\theta}_i^{t,k+1} - \boldsymbol{\theta}_i^{t,k} \mid \mathcal{F}_i^{t,k} \right] = -\eta \left((1 - \gamma)\Delta_G^t + \gamma \nabla f_i(\boldsymbol{\theta}_i^{t,k}) \odot \vartheta_i^{t,k} \right)$. Then we have

$$\begin{aligned} \mathbb{E} \left[\|\xi_i^{t,j} - \xi_i^{t,j-1}\|^2 \right] &\leq \frac{1}{\epsilon^2} \eta^2 L^2 \gamma^2 \mathbb{E} \left[\|\boldsymbol{\theta}_i^{t,j} - \boldsymbol{\theta}_i^{t,j-1}\|^2 \right] \\ &\leq \frac{1}{\epsilon^2} \eta^2 L^2 \gamma^2 \left(\eta^2 \gamma^2 \sigma_l^2 + \mathbb{E} \left[\|\xi_i^{t,j-1}\|^2 \right] \right). \end{aligned}$$

For any $1 \leq j \leq k-1 \leq K-2$, using $\eta L \leq \frac{1}{\gamma K} \leq \frac{1}{\gamma(k+1)}$, we have

$$\begin{aligned} \mathbb{E} \left[\|\xi_i^{t,j}\|^2 \right] &\leq \left(1 + \frac{1}{k}\right) \mathbb{E} \left[\|\xi_i^{t,j-1}\|^2 \right] + (1+k) \mathbb{E} \left[\|\xi_i^{t,j} - \xi_i^{t,j-1}\|^2 \right] \\ &\leq \left(1 + \frac{2}{k}\right) \mathbb{E} \left[\|\xi_i^{t,j-1}\|^2 \right] + (k+1) \frac{1}{\epsilon^2} L^2 \eta^4 \gamma^4 \sigma_l^2 \\ &\leq e^2 \mathbb{E} \left[\|\xi_i^{t,0}\|^2 \right] + 4\frac{1}{\epsilon^2} k^2 L^2 \eta^4 \gamma^4 \sigma_l^2. \end{aligned}$$

where the last inequality is by unrolling the recursive bound and using $(1 + \frac{2}{k})^k \leq e^2$. By Lemma 1, it holds that for $k \geq 2$,

$$\begin{aligned} \mathbb{E} \left[\|\boldsymbol{\theta}_i^{t,k} - \boldsymbol{\theta}^t\|^2 \right] &\leq 2\mathbb{E} \left[\left\| \sum_{j=0}^{k-1} \xi_i^{t,j} \right\|^2 \right] + 2\frac{1}{\epsilon^2} k\eta^2 \gamma^2 \sigma_l^2 \\ &\leq 2k \sum_{j=0}^{k-1} \mathbb{E} \left[\|\xi_i^{t,k}\|^2 \right] + 2\frac{1}{\epsilon^2} k\eta^2 \gamma^2 \sigma_l^2 \\ &\leq 2e^2 k^2 \mathbb{E} \left[\|\xi_i^{t,0}\|^2 \right] + 2\frac{1}{\epsilon^2} k\eta^2 \gamma^2 \sigma_l^2 (1 + 4k^3 L^2 \eta^2 \gamma^2). \end{aligned}$$

This is also valid for $k = 0, 1$. Summing up over i and k , we finish the proof. □

Lemma 6. *If $288e(\eta KL)^2 ((1 - \gamma)^2 + e(\gamma\gamma LR)^2) \leq 1$, then it holds for $t \geq 0$ that*

$$\sum_{t=0}^{R-1} \Xi_t \leq \frac{1}{72eK^2 L^2} \sum_{t=-1}^{R-2} \left(\mathcal{E}_t + \mathbb{E} \left[\|\nabla f(\boldsymbol{\theta}^t)\|^2 \right] \right) + 2\eta^2 \gamma^2 \frac{1}{\epsilon^2} eRG_0.$$

Proof. Note that $\xi_i^{t,0} = -\eta \left((1 - \gamma)\Delta_G^t + \gamma \nabla f_i(\boldsymbol{\theta}^t) \odot \vartheta_i^{t,k} \right)$,

$$\frac{1}{N} \sum_{i=1}^N \|\xi_i^{t,0}\|^2 \leq 2\eta^2 \left((1 - \gamma)^2 \|\Delta_G^t\|^2 + \gamma^2 \frac{1}{N} \sum_{i=1}^N \|\nabla f_i(\boldsymbol{\theta}^t)\|^2 \right).$$

Using Young's inequality, we have for any $q > 0$ that

$$\begin{aligned} \mathbb{E} \left[\|\nabla f_i(\boldsymbol{\theta}^t)\|^2 \right] &\leq (1+q)\mathbb{E} \left[\|\nabla f_i(\boldsymbol{\theta}^{t-1})\|^2 \right] + (1+q^{-1})L^2\mathbb{E} \left[\|\boldsymbol{\theta}^t - \boldsymbol{\theta}^{t-1}\|^2 \right] \\ &\leq (1+q)\mathbb{E} \left[\|\nabla f_i(\boldsymbol{\theta}^{t-1})\|^2 \right] + 2(1+q^{-1})\gamma^2L^2 \left(\mathcal{E}_{t-1} + \mathbb{E} \left[\|\nabla f(\boldsymbol{\theta}^{t-1})\|^2 \right] \right) \\ &\leq (1+q)^t\mathbb{E} \left[\|\nabla f_i(\boldsymbol{\theta}^0)\|^2 \right] + \frac{2}{q}\gamma^2L^2 \sum_{j=0}^{t-1} \left(\mathcal{E}_j + \mathbb{E} \left[\|\nabla f(\boldsymbol{\theta}^j)\|^2 \right] \right) (1+q)^{t-j}. \end{aligned}$$

Take $q = \frac{1}{t}$ and we have

$$\mathbb{E} \left[\|\nabla f_i(\boldsymbol{\theta}^t)\|^2 \right] \leq e\mathbb{E} \left[\|\nabla f_i(\boldsymbol{\theta}^0)\|^2 \right] + 2e(t+1)\gamma^2L^2 \sum_{j=0}^{t-1} \left(\mathcal{E}_j + \mathbb{E} \left[\|\nabla f(\boldsymbol{\theta}^j)\|^2 \right] \right). \quad (16)$$

Note that this inequality is valid for $t = 0$. Therefore, using (16), we have

$$\begin{aligned} \sum_{t=0}^{R-1} \Xi_t &\leq \sum_{t=0}^{R-1} 2\eta^2\mathbb{E} \left[(1-\gamma)^2 \|\Delta_G^t\|^2 + \gamma^2 \frac{1}{\epsilon^2} \frac{1}{N} \sum_{i=1}^N \|\nabla f_i(\boldsymbol{\theta}^t)\|^2 \right] \\ &\leq \sum_{t=0}^{R-1} 2\eta^2 \left(2(1-\gamma)^2 \left(\mathcal{E}_{t-1} + \mathbb{E} \left[\|\nabla f(\boldsymbol{\theta}^{t-1})\|^2 \right] \right) + \gamma^2 \frac{1}{\epsilon^2} \frac{1}{N} \sum_{i=1}^N \mathbb{E} \left[\|\nabla f_i(\boldsymbol{\theta}^t)\|^2 \right] \right) \\ &\leq \sum_{t=0}^{R-1} 4\eta^2(1-\gamma)^2 \left(\mathcal{E}_{t-1} + \mathbb{E} \left[\|\nabla f(\boldsymbol{\theta}^{t-1})\|^2 \right] \right) \\ &\quad + 2\eta^2\gamma^2 \frac{1}{\epsilon^2} \sum_{t=0}^{R-1} \left(\frac{e}{N} \sum_{i=1}^N \mathbb{E} \left[\|\nabla f_i(\boldsymbol{\theta}^0)\|^2 \right] + 2e(t+1)(\gamma L)^2 \sum_{j=0}^{t-1} \left(\mathcal{E}_j + \mathbb{E} \left[\|\nabla f(\boldsymbol{\theta}^j)\|^2 \right] \right) \right) \\ &\leq 4\eta^2(1-\gamma)^2 \sum_{t=0}^{R-1} \left(\mathcal{E}_{t-1} + \mathbb{E} \left[\|\nabla f(\boldsymbol{\theta}^{t-1})\|^2 \right] \right) \\ &\quad + 2\eta^2\gamma^2 \frac{1}{\epsilon^2} \left(eRG_0 + 2e(\gamma LR)^2 \sum_{t=0}^{R-2} \left(\mathcal{E}_t + \mathbb{E} \left[\|\nabla f(\boldsymbol{\theta}^t)\|^2 \right] \right) \right). \end{aligned}$$

Rearranging the equation and applying the upper bound of η , we finish the proof. \square

Theorem 3 (Convergence for non-convex functions). *Under Assumption A.1 and A.2 and A.3, if we take $g^0 = 0$,*

$$\begin{aligned} \gamma &= \min \left\{ \sqrt{\frac{SKL\Delta\epsilon^2}{\sigma_i^2 R}}, \text{ for any constant } c \in (0, 1], \quad \gamma = \min \left\{ \frac{1}{24LG_g}, \frac{\gamma}{6L} \right\}, \right. \\ \eta KL &\lesssim \min \left\{ 1, \frac{1}{\gamma\gamma LR}, \left(\frac{L\Delta}{G_0\gamma^3 R} \right)^{1/2}, \frac{1}{(\gamma N)^{1/2}}, \frac{1}{(\gamma^3 NK)^{1/4}} \right\}. \end{aligned}$$

then DP-FedAdamW converges as

$$\frac{1}{R} \sum_{t=0}^{R-1} \mathbb{E} \left[\|\nabla f(\boldsymbol{\theta}^t)\|^2 \right] \lesssim \sqrt{\frac{L\Delta\sigma_i^2}{SKR}} + \frac{L\Delta}{R} + \frac{\sigma^2 G_g^2}{s^2 R^2}.$$

Here $G_0 := \frac{1}{N} \sum_{i=1}^N \|\nabla f_i(\boldsymbol{\theta}^0)\|^2$.

Proof. Combining Lemma 3 and 4, we have

$$\begin{aligned}\mathcal{E}_t &\leq \left(1 - \frac{8\gamma}{9}\right) \mathcal{E}_{t-1} + 4\frac{(\gamma L)^2}{\gamma} \mathbb{E} \left[\|\nabla f(\boldsymbol{\theta}^{t-1})\|^2 \right] + \frac{2\gamma^2\sigma_l^2}{SK\epsilon^2} \\ &\quad + 4\frac{\gamma}{\epsilon^2} L^2 \left(2eK^2\Xi_t + K\eta^2\gamma^2 \frac{1}{\epsilon^2} \sigma_l^2 (1 + 2K^3L^2\eta^2\gamma^2) \right),\end{aligned}$$

and

$$\mathcal{E}_0 \leq (1 - \gamma)\mathcal{E}_{-1} + \frac{2\gamma^2\sigma_l^2}{SK\epsilon^2} + 4\gamma\frac{1}{\epsilon^2} L^2 \left(2eK^2\Xi_0 + K\eta^2\gamma^2 \frac{1}{\epsilon^2} \sigma_l^2 (1 + 2K^3L^2\eta^2\gamma^2) \right).$$

Summing over t from 0 to $R - 1$ and applying Lemma 6,

$$\begin{aligned}\sum_{t=0}^{R-1} \mathcal{E}_t &\leq \left(1 - \frac{8\gamma}{9}\right) \sum_{t=-1}^{R-2} \mathcal{E}_t + 4\frac{(\gamma L)^2}{\gamma} \sum_{t=0}^{R-2} \mathbb{E} \left[\|\nabla f(\boldsymbol{\theta}^t)\|^2 \right] + 2\frac{\gamma^2\sigma_l^2}{SK\epsilon^2} R \\ &\quad + 4\gamma\frac{1}{\epsilon^2} L^2 \left(2eK^2 \sum_{t=0}^{R-1} \Xi_t + RK\eta^2\gamma^2 \frac{1}{\epsilon^2} \sigma_l^2 (1 + 2K^3L^2\eta^2\gamma^2) \right) \\ &\leq \left(1 - \frac{7\gamma}{9}\right) \sum_{t=-1}^{R-2} \mathcal{E}_t + \left(4\frac{(\gamma L)^2}{\gamma} + \frac{\gamma}{9}\right) \sum_{t=-1}^{R-2} \mathbb{E} \left[\|\nabla f(\boldsymbol{\theta}^t)\|^2 \right] + 16\gamma^3 \frac{1}{\epsilon^4} (e\eta KL)^2 RG_0 \\ &\quad + \frac{2\gamma^2\sigma_l^2}{SK\epsilon^2} R + 4\gamma^3 \frac{1}{\epsilon^4} (\eta KL)^2 \left(\frac{1}{K} + 2(\eta KL\gamma)^2 \right) \sigma_l^2 R \\ &\leq \left(1 - \frac{7\gamma}{9}\right) \sum_{t=-1}^{R-2} \mathcal{E}_t + \frac{2\gamma}{9} \sum_{t=-1}^{R-2} \mathbb{E} \left[\|\nabla f(\boldsymbol{\theta}^t)\|^2 \right] + 16\gamma^3 \frac{1}{\epsilon^4} (e\eta KL)^2 RG_0 + \frac{4\gamma^2\sigma_l^2}{SK\epsilon^2} R.\end{aligned}$$

Here in the last inequality we apply

$$4\gamma\frac{1}{\epsilon^4} (\eta KL)^2 \left(\frac{1}{K} + 2(\eta KL\gamma)^2 \right) \leq \frac{2}{NK} \quad \text{and} \quad \gamma L \leq \frac{\gamma}{6}.$$

Therefore,

$$\sum_{t=0}^{R-1} \mathcal{E}_t \leq \frac{9}{7\gamma} \mathcal{E}_{-1} + \frac{2}{7} \mathbb{E} \left[\sum_{t=-1}^{R-2} \|\nabla f(\boldsymbol{\theta}^t)\|^2 \right] + \frac{144}{7} \frac{1}{\epsilon^4} (e\eta KL)^2 G_0 R + \frac{36\gamma\sigma_l^2}{7SK\epsilon^2} R.$$

Combine this inequality with Lemma 3 and we get

$$\frac{1}{\gamma} \mathbb{E} [f(\boldsymbol{\theta}^t) - f(\boldsymbol{\theta}^0)] \leq -\frac{1}{7} \sum_{t=0}^{R-1} \mathbb{E} \left[\|\nabla f(\boldsymbol{\theta}^t)\|^2 \right] + \frac{39}{56\gamma} \mathcal{E}_{-1} + \frac{78}{7} \frac{1}{\epsilon^4} (e\eta KL)^2 G_0 R + \frac{39\gamma\sigma_l^2}{14SK\epsilon^2} R.$$

Finally, noticing that $g^0 = 0$ implies $\mathcal{E}_{-1} \leq 2L(f(\boldsymbol{\theta}^0) - f^*) = 2L\Delta$, we obtain

$$\begin{aligned}\frac{1}{R} \sum_{t=0}^{R-1} \mathbb{E} \left[\|\nabla f(\boldsymbol{\theta}^t)\|^2 \right] &\lesssim \frac{L\Delta}{\gamma LR} + \frac{\mathcal{E}_{-1}}{\gamma T} + (\gamma\eta KL)^2 \frac{1}{\epsilon^4} G_0 + \frac{\gamma\sigma_l^2}{SK\epsilon^2} + \frac{\sigma^2 G_g^2}{s^2 T^2} \\ &\lesssim \frac{L\Delta}{T} + \frac{L\Delta}{\gamma T} + \frac{\gamma\sigma_l^2}{SK\epsilon^2} + (\gamma\eta KL)^2 G_0 \frac{1}{\epsilon^4} + \frac{\sigma^2 G_g^2}{s^2 T^2} \\ &\lesssim \frac{L\Delta}{T} + \sqrt{\frac{L\Delta\sigma_l^2}{SKT\epsilon^2}} + \frac{\sigma^2 G_g^2}{s^2 T^2}.\end{aligned}$$

□